

Using Gaussian Splats to Create High-Fidelity Facial Geometry and Texture

Haodi He
Epic Games, Stanford University
hardyhe@stanford.edu

Jihun Yu
Epic Games
jihun.yu@epicgames.com

Ronald Fedkiw
Epic Games, Stanford University
rfedkiw@stanford.edu

Abstract

We leverage increasingly popular three-dimensional neural representations in order to construct a unified and consistent explanation of a collection of uncalibrated images of the human face. Our approach utilizes Gaussian Splatting, since it is more explicit and thus more amenable to constraints than NeRFs. We leverage segmentation annotations to align the semantic regions of the face, facilitating the reconstruction of a neutral pose from only 11 images (as opposed to requiring a long video). We soft constrain the Gaussians to an underlying triangulated surface in order to provide a more structured Gaussian Splat reconstruction, which in turn informs subsequent perturbations to increase the accuracy of the underlying triangulated surface. The resulting triangulated surface can then be used in a standard graphics pipeline. In addition, and perhaps most impactful, we show how accurate geometry enables the Gaussian Splats to be transformed into texture space where they can be treated as a view-dependent neural texture. This allows one to use high visual fidelity Gaussian Splatting on any asset in a scene without the need to modify any other asset or any other aspect (geometry, lighting, renderer, etc.) of the graphics pipeline. We utilize a relightable Gaussian model to disentangle texture from lighting in order to obtain a delit high-resolution albedo texture that is also readily usable in a standard graphics pipeline. The flexibility of our system allows for training with disparate images, even with incompatible lighting, facilitating robust regularization. Finally, we demonstrate the efficacy of our approach by illustrating its use in a text-driven asset creation pipeline.

1. Introduction

Facial avatars are essential for a wide range of applications including virtual reality, video conferencing, gaming, feature films, etc. As virtual interactions become more prevalent, the demand for compelling digital representations of human faces will continue to grow. A person’s face avatar should accurately reflect their identity, while also being controllable, relightable, and efficient enough to use in real-time applica-

tions. These requirements have driven significant research endeavors in computer vision, computer graphics, and machine learning. However, it is still challenging to create such avatars in a scalable and democratized way, i.e. with commodity hardware and limited input data and without using multiple calibrated cameras or a light-stage.

Neural Radiance Fields (NeRFs) [74] have become increasingly prevalent in both computer vision and computer graphics due to their impressive ability to reconstruct and render 3D scenes from 2D image collections. In particular, various authors have achieved impressive photorealistic results on 3D human faces. The implicit nature of the NeRF representation facilitates high-quality editing (see e.g. [21]), since it keeps edits both non-local and smooth (similar to splines, but dissimilar to triangulated surfaces). In addition, the regularization provided by the low dimensional latent space keeps edits of faces looking like faces. It is far more difficult for non-expert users to edit triangulated surface geometry and textures directly.

Although only recently proposed, Gaussian Splatting [53] has quickly become remarkably popular. Its explicit nature makes it significantly more amenable to various constraints than other (typically implicit) neural models. Importantly, NeRFs and Gaussian Splatting complement each other, as one can edit a NeRF representation before converting it into a Gaussian Splatting model for various downstream tasks that would benefit from having a more structured and constrained representation.

The standard graphics pipeline has been refined over decades via both software and hardware optimizations and has become quite mature, especially for real-time applications. In fact, in spite of the maturity and impact of ray tracing, it has only recently been somewhat incorporated into gaming consoles and other real-time applications. Silicon chip development is often a zero-sum game where adding one capability necessarily removes another. However, ray tracing has been embraced in non-realtime applications and is often used to create content for real-time applications. It is not a stretch to assume that neural rendering methods will be treated similarly. Thus, converting neural models, such as Gaussian Splatting, into triangulated surfaces with tex-

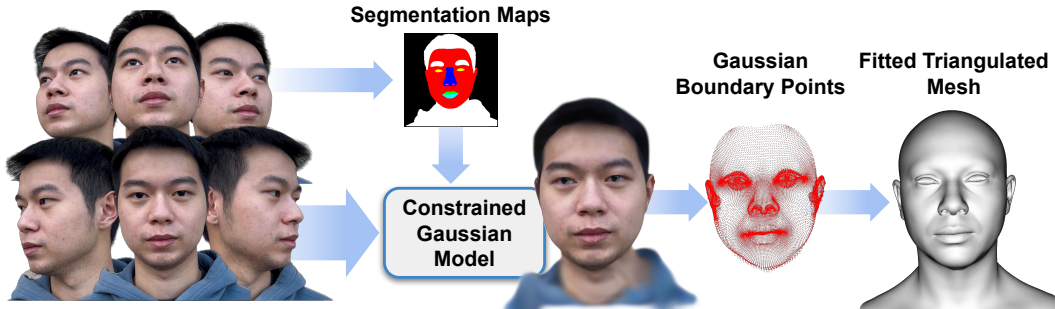


Figure 1. Using a small number of self-captured uncalibrated multi-view images, we use segmentation annotations along with size and shape constraints to force the Gaussians to move instead of deform. In addition, soft constraints are used to keep the Gaussians tightly coupled and close to the triangulated surface. After training, in a post process, the triangulated surface is deformed to better approximate the Gaussian reconstruction.

tures disentangled from lighting necessarily increases their immediate impact on real-time computer graphics applications. In this work, we address this by introducing a pipeline that transforms a Gaussian Splatting model trained with self-captured uncalibrated multi-view images into a triangulated surface with de-lit textures.

Our method offers significant advantages over traditional mesh-based geometry reconstruction, since it does not rely on the ability of advanced shading models to overcome the domain gap between synthetic and real images. Instead, neural rendering is used to close the domain gap, while constraints are used to tightly connect the neural rendering degrees of freedom to an explicit triangulated surface. The Gaussian Splatting model is modified to more tightly couple it to the triangulated surface in two ways: segmentation annotations along with size and shape constraints are used to force the Gaussians to move (instead of deform) in order to explain the data, and soft constraints are used to keep the Gaussians tightly coupled and close to the triangulated surface. After training, in a post process, the triangulated surface is deformed to better approximate the Gaussian reconstruction. See Fig. 1 and Fig. 2.

In order to obtain a de-lit texture with albedo disentangled from normal and lighting, without the need of a light-stage, we regularize this underconstrained problem by utilizing a PCA representation of a mesh-based facial texture derived from the Metahuman dataset [33]. We optimize the PCA coefficients to reconstruct albedo as faithfully as possible, while minimizing reliance on a Relightable Gaussian Splatting model that is used to capture residual differences between a target image and a rendering of the textured mesh.

In summary, we obtain an accurate triangulated surface reconstruction with de-lit high-resolution textures, compatible with a standard graphics pipeline. Moreover, we demonstrate the efficacy of our approach by illustrating its use in a text-driven asset creation pipeline. Key contributions include:

- We propose two key modifications of Gaussian Splatting in order to enable accurate triangulated surface reconstruction: Soft constraints encourage Gaussians to be more tightly coupled to the underlying mesh, so that Gaussian perturbations can more accurately drive mesh deformation. Segmentation annotations supervise the Gaussians, so that they do not attempt to explain regions of the target image

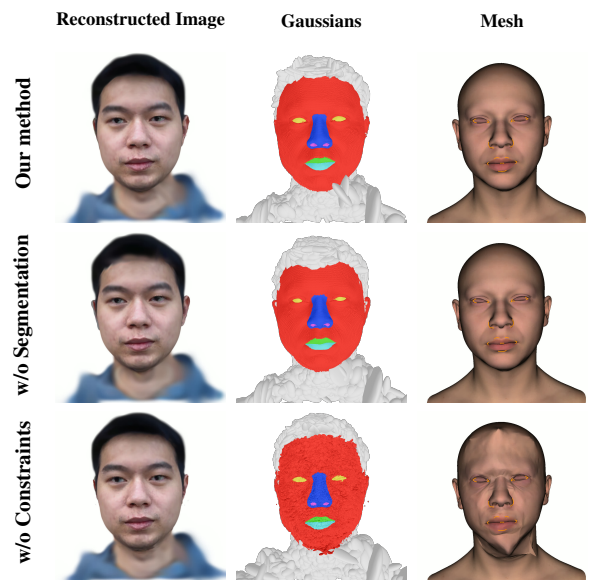


Figure 2. The ground-truth is well-reconstructed (column 1) not only by our method but also in the ablation tests where segmentation supervision (row 2) and constraints (row 3) have been omitted. Omitting segmentation supervision allows the Gaussians to incorrectly explain regions of the image that their triangles should not be associated with (compare row 2 column 2 to row 1 column 2), resulting in spurious geometry (row 2 column 3). Omitting soft constraints disconnects the Gaussians from their triangles resulting in very spurious geometry (row 3 column 3).

that they should not be associated with.

- We present a method that disentangles albedo textures from lighting and normals. The PCA coefficients of the textured mesh are optimized to capture as much albedo color as possible while minimizing the contributions from the relightable Gaussians that are used to capture differences between the synthetic rendering of the mesh and the target image.
- Our method avoids the need of controlled capture setups and instead requires only commodity hardware and limited number of views. In fact, the flexibility of our approach allows for joint training using data from different capture setups; as an example, we combine images from our capture method with those obtained from so-called flashlight capture (see e.g. [44]).
- Finally, and perhaps most importantly, we illustrate that the geometry obtained via our pipeline is accurate enough to use in conjunction with a view-dependent neural texture. In particular, we propose a novel Gaussian Splatting approach to view-dependent neural textures, emphasizing that this enables the utilization of high visual fidelity Gaussian Splatting on any asset in a scene without the need to modify any other asset or any other aspect (geometry, lighting, renderer, etc.) of the graphics pipeline.

2. Related Work

NeRFs: Generally speaking, NeRFs disentangle camera intrinsics and extrinsics from facial and other representations by predicting color and density for volumetric ray marching. Some frameworks utilize parameterized models such as 3DMM (e.g. [34, 47, 127]), FLAME (e.g. [2, 30]), or related parameterization (e.g. [36]) as inputs; then, expression parameters are used to morph a neutral expression-less face from a canonical space into the scene (e.g. [95]). Although NeRFs do not disentangle geometry, coarse geometry is sometimes used to drive the morph (e.g. [5, 128]). Some works (e.g. [88, 114]) have aimed to relight NeRFs, but the coarse geometry and the entanglement between geometry and texture hinders the ability to disentangle lighting in a manner that facilitates the incorporation of NeRFs into a standard graphics pipeline. Still, the implicit representation and the latent space regularization make NeRFs a powerful editing framework (e.g. [21, 51, 60, 92]). The latent space regularization also makes NeRFs good candidates for democratized personal avatar generation using only a few images or a quick phone scan (e.g. [11, 12, 14, 114]).

Gaussian Splatting: Similar to NeRFs, Gaussian Splatting methods use expression parameters to deform a canonical space representation (e.g. [103, 110, 111, 121]), often with the aid of a triangulated surface (e.g. [17, 81, 90, 94]). In fact, triangulated surfaces can be used to parent Gaussians for other structures as well, such as hair (e.g. [102]).

Gaussian Splatting has surpassed NeRFs in a number of areas, including for democratized personal avatar generation (e.g. [19, 45, 65, 68, 89]). We utilize a relightable Gaussian Splatting model (e.g. [61, 87]) in order to disentangle texture from lighting. Most similar to our approach, [64] leverages Gaussian Splatting to reconstruct a sequence of triangulated surface meshes with high-resolution textures from multi-view light stage videos; in contrast, our method does not require a controlled capture setup and enables de-lighting of the texture.

Other Neural Representations: Besides NeRFs and Gaussian Splatting, there are number of other neural approaches. The vast majority of these are based on GANs [41], see e.g. [66, 101]. Most of the three-dimensional approaches rely on implicit formulations and SDFs (e.g. [40, 44, 115, 122]), although some approaches do use explicit geometry (see e.g. [123], which uses a point-based approach). Several works (e.g. [42, 70, 91, 102]) employ meshes with view and expression dependent neural textures, following [98], to further enhance photorealism.

Geometry Reconstruction: Mesh-based geometry reconstruction typically relies on PCA for regularization to combat noise. Popular examples include 3DMM [7], FLAME [63], and other variants (e.g. [6, 10, 13, 79, 104]). Some methods compute additional per-vertex deformations that are added on top of the parameterized geometry. Older approaches use various approximations to rendering (e.g. [37, 38]), while newer approaches use either a fully differentiable ray tracer (e.g. [29, 104]) or neural rendering (e.g. [42, 70, 98]). Machine learning approaches rely on the ability to pretrain a model on large datasets (e.g. [3, 13, 20, 69, 83, 85, 86, 108, 116, 125]), inferring mesh parameters using either a single view (e.g. [15, 56, 85, 96, 99, 100, 109, 113, 118]) or multiple views (e.g. [9, 26, 97]).

Texture and Lighting: Although chrome spheres have been used to estimate on-set lighting conditions for feature films for three decades (see e.g. [23]) and the main ideas behind them originated even two decades before that (see e.g. [8, 75]), much of the prior work still does not disentangle texture from lighting. Of those that do aim to obtain de-lit textures and lighting estimates, the higher-end efforts utilize a light-stage (e.g. [24, 39, 71]), see for example [64, 87]. Using large-scale light-stage datasets (e.g. [57, 62]), neural networks can be trained to predict de-lit textures, surface normals, and lighting conditions (e.g. [58, 76, 93]). See also [54, 78, 107, 112]. In addition to approaches that leverage a light-stage or light-stage data, a number of approaches aim to disentangle texture from lighting for in-the-wild single-view images under unconstrained conditions: [28, 29, 100] incorporate physical or statistical regularizations, [48, 49] model shadows to better separate shading from albedo, and [4, 124] generate pseudo ground-truth data

to aid training. Similarly, various approaches utilize multi-view images (e.g. [6, 61, 105, 123]).

3. Preliminaries

3.1. Gaussian Splatting

Gaussian Splatting [53] represents a scene using a collection of 3D Gaussian primitives,

$$G(\mathbf{x}) = e^{-\frac{1}{2}(\mathbf{x}-\boldsymbol{\mu})^\top \Sigma^{-1}(\mathbf{x}-\boldsymbol{\mu})} \quad (1)$$

with mean position $\boldsymbol{\mu} \in \mathbb{R}^3$ and covariance matrix $\Sigma \in \mathbb{R}^{3 \times 3}$. The covariance matrix is constructed via $\Sigma = RSS^\top R^\top$ with diagonal anisotropic scaling S and rotation R . During rendering, each 3D Gaussian is projected to a 2D Gaussian in screen space to obtain $\boldsymbol{\mu}_{2D}$ and $\Sigma_{2D} = JW\Sigma W^\top J^\top$ where W is the viewing transformation and J is the Jacobian of the projective transformation evaluated at $W\boldsymbol{\mu}$. Given an opacity $\alpha \in [0, 1]$, the Gaussian makes a contribution of

$$w(p) = \alpha e^{-\frac{1}{2}(p-\boldsymbol{\mu}_{2D})^\top \Sigma_{2D}^{-1}(p-\boldsymbol{\mu}_{2D})} \quad (2)$$

at pixel p . Pixel colors are computed using front-to-back alpha compositing via

$$\sum_i \left(\prod_{j < i} (1 - w_j(p)) \right) w_i(p) \mathbf{c}_i(\mathbf{v}(\boldsymbol{\mu}_i)) \quad (3)$$

where the viewing direction \mathbf{v} is computed using the mean position of the Gaussian, and the view-dependent color \mathbf{c}_i is computed using \mathbf{v} and the Gaussian’s learned per-channel spherical harmonic coefficients.

3.2. Gaussian Avatars

Gaussian Avatars [81] represent deformable head models by attaching Gaussians to the triangles of a mesh. The position and covariance of each Gaussian is defined in the local coordinate system of its parent triangle and driven by the triangle’s motion via

$$\boldsymbol{\mu}(\theta) = R(\theta)\boldsymbol{\mu}_{\text{local}} + \mathbf{T}(\theta) \quad (4)$$

$$\Sigma(\theta) = s(\theta)^2 R(\theta)\Sigma_{\text{local}}R(\theta)^\top \quad (5)$$

where R , \mathbf{T} , and s are defined for each frame via construction. The translation \mathbf{T} is set to be equal to the centroid of the triangle. The first and second consistently chosen edges are used to construct an orthogonal basis for the plane of the triangle via Gram-Schmidt; then, columns of R are defined using those two orthogonal vectors and their cross product. The (scalar) scale factor s is defined by averaging the length of a consistently chosen edge and its altitude. Ideally, R , \mathbf{T} , and s capture a significant portion of $\boldsymbol{\mu}_{\text{local}}$ and Σ_{local} , allowing the learned $\boldsymbol{\mu}_{\text{local}}$ and Σ_{local} to focus on the fine-scale

geometric variations that are not captured by the triangle mesh. Moreover, using the same canonical space version of $\boldsymbol{\mu}_{\text{local}}$ and Σ_{local} for every frame adds regularization to combat overfitting.

Following [81], we regularize the local scaling (S in Sec. 3.1, which is S_{local} in Σ_{local}) via

$$\mathcal{L}_{\text{scale}} = \left\| \sum_i \max\left(\hat{\mathbf{e}}_i^\top S_{\text{local}} \hat{\mathbf{e}}_i, \epsilon_{\text{scale}}\right) \hat{\mathbf{e}}_i \right\|_2 \quad (6)$$

aiming to shrink the diagonal entries of S_{local} that are larger than $\epsilon_{\text{scale}} = 0.6$. Note, $\hat{\mathbf{e}}_i$ are the standard basis vector in \mathbb{R}^3 .

3.3. Relightable Gaussian Avatars

Relightable Gaussian Avatars [87] modify the color in Eq 3, replacing it with the sum of a diffuse and a specular term. For each of the three color channels, the diffuse component is computed by integrating over the surface of a sphere

$$c^{\text{diffuse}} = \rho \int_{\mathbb{S}} L(\boldsymbol{\omega}) d(\boldsymbol{\omega}) d\boldsymbol{\omega} = \rho \sum_k L_k d_k \quad (7)$$

where ρ is the learned albedo, \mathbf{L} is the environment lighting, and \mathbf{d} is a learned radiance transfer function. The integral in Eq. 7 is simplified into a summation by representing both \mathbf{L} and \mathbf{d} via their spherical harmonics approximations. The view-dependent specular term is defined by

$$\begin{aligned} c^{\text{specular}}(\boldsymbol{\mu}_i, \mathbf{n}_i, \sigma_i, \tilde{\mathbf{v}}_i) \\ = \tilde{\mathbf{v}}_i(\mathbf{v}(\boldsymbol{\mu}_i)) \int_{\mathbb{S}} \mathbf{L}(\boldsymbol{\omega}) G(\boldsymbol{\omega}, \mathbf{v}_r(\mathbf{v}(\boldsymbol{\mu}_i), \mathbf{n}_i), \sigma_i) d\boldsymbol{\omega} \end{aligned} \quad (8)$$

where $\mathbf{v}_r = 2(\mathbf{v} \cdot \mathbf{n}) \mathbf{n} - \mathbf{v}$ is the mirror reflection direction about a learned surface normal \mathbf{n} , and the spherical Gaussian kernel G depends on a learned specular sharpness σ . Note that [87] combined a number of view-dependent terms and aggressively dropped their dependence on $\boldsymbol{\omega}$ so that they could be pulled out of the integral and be represented by the learnable $\tilde{\mathbf{v}}$.

4. Method

To summarize, our method reconstructs a (de-lit) textured triangulated surface mesh, suitable for use in a standard graphics pipeline, from either a short monocular video or a set of images. In Section 4.1, we describe the data acquisition and initialization steps, which include using landmark detection in order to estimate head pose and to generate a coarse approximation to the triangulated surface. In Section 4.2, we discuss how we use soft constraints and segmentation annotations in order to more tightly couple the Gaussian Splatting model to the underlying triangulated surface. In Section 4.3, we discuss how our modified Gaussian Splatting model can



Figure 3. The 11 predefined target head poses used for reconstruction.

be used to drive deformation of the underlying triangulated surface in order to obtain detailed and representative reconstructed geometry. In Section 4.4, we demonstrate that the geometry obtained via our pipeline is accurate enough to use in conjunction with a view-dependent neural texture. In Section 4.5 and 4.6, we explain how we generate high-resolution textures disentangled from lighting. Finally, in Section 4.7 we wrap up with the discussion on how to convert our final result into a MetaHuman framework so that it can be used in wide variety of applications.

4.1. Data Acquisition and Initialization

We capture a 4K-resolution monocular video of the subject using the rear camera of an iPhone 14 held in a fixed position. During recording, the subject slowly rotates their head while maintaining a neutral expression. This is done outdoors in shaded conditions in order to minimize harsh lighting and specular highlights. Afterwards, each video frame is center-cropped to a resolution of 2160×2160 pixels. A pretrained landmark detection network [35] is used to infer both facial and skull landmarks on each frame. Assuming the camera is fixed (as it is in our data acquisition), the skull landmarks are used to estimate the head pose (rotation and translation) for each frame by comparing the inferred landmarks with corresponding landmarks on a 3D canonical template. Although this assumes that the subject and the template have the same size head, we only require a rough pose estimation during the initialization stage.

Eleven predefined target head poses are chosen for the reconstruction, shown in Fig. 3. Given a predefined target head pose, we select the closest non-blurry frame. Closeness is measured by comparing the estimated rotation to the target rotation, and blurriness is measured using the variance of the Laplacian of the pixel values in the grayscale image (as is typical, see e.g. [80]). Weights are used to combine closeness and blurriness into an objective function, so that the process can be automated via minimization.

Starting with a front-facing image, we obtain a rough estimation to depth via [1]. Then, the image, depth estimate, and landmarks are used as input into the MetaHuman Animator [35] in order to obtain a triangulated surface. The resulting mesh is topologically consistent with other MetaHumans making it compatible with modern graphics pipelines;

however, it does not well-represent the subject, given all the rough approximation used in the process. On the other hand, it does provide a good initial guess for Gaussian Splatting. To simplify the model, we remove the triangles associated with the teeth, inner mouth, and eyelashes resulting in a face mesh with 47,944 triangles.

4.2. Modified Gaussian Splatting Model

Similar to Gaussian Avatars [81], we attach Gaussians to the triangles of the mesh; however, we do not jointly optimize the triangulated surface along with the Gaussian parameters during training. This decoupling allows us to more readily leverage various improvements in Gaussian Splatting as they become available. It also allows us to independently use mesh regularization and other mesh-based considerations without adversely affecting the Gaussian Splatting. We assign exactly one Gaussian to each mesh triangle and disable both densification and pruning during training. This one-to-one correspondence between Gaussians and mesh triangles makes geometry regularization and subsequent surface reconstruction more straightforward.

It is worth noting two other approaches that modify the Gaussian Splatting model in order to facilitate triangulated surface reconstruction. [50] uses flattened two-dimensional Gaussians along with depth distortion and normal consistency regularization terms, and [43] uses SDF-based regularization. These modifications all encourage the Gaussians to better align with the surfaces they represent.

4.2.1. Soft Constraints for Geometric Regularization

We promote local geometric consistency of the Gaussians by introducing soft regularization terms that encourage specific geometric features to not vary too much across the mesh. This is accomplished via

$$\mathcal{L}_{\text{reg}} = \sum_i \left\| \mathbf{z}_i - \frac{1}{|\mathcal{E}(i)|} \sum_{j \in \mathcal{E}(i)} \mathbf{z}_j \right\|^2 \quad (9)$$

where $\mathcal{E}(i)$ represents Gaussians associated with mesh triangles that share an edge with the triangle containing Gaussian i . Note that $i \notin \mathcal{E}(i)$. \mathcal{L}_{reg} encourages each \mathbf{z}_i to be equal to the average \mathbf{z} value of its neighbors. This incorrectly weighted Laplacian smoothing (see [27]) is more similar to a standard deviation with the global mean replaced by local means.

To better regularize the eyeballs, which are disconnected from the face mesh, we identify bi-directional nearest neighbor pairs between triangle centroids of the eyeballs and triangle centroids of the face mesh; then, Gaussians associated with these nearest neighbor pairs are included in the construction of \mathcal{E} .

Center Displacements. Here, we consider the displacement between each Gaussian center μ_i and its corresponding mesh

triangle centroid \mathbf{T}_i as the geometric feature of interest via $\mathbf{z}_i = \boldsymbol{\mu}_i - \mathbf{T}_i$ in Eq. 9 in order to obtain $\mathcal{L}_{\text{reg}}^{\text{center}}$. This aims to keep Gaussians as close to the mesh as their neighbors are, helping to regularize subsequent mesh deformation that will be driven in part by these offsets.

Local Normal.

Here, we consider the geometric feature $\mathbf{z}_i = \mathbf{n}_{i,\text{local}}$, the local normal of Gaussian i , in Eq. 9 in order to obtain $\mathcal{L}_{\text{reg}}^{\text{normal}}$. This aims to keep disagreements in the normal direction between Gaussians and the mesh smoothly varying over the mesh, again helping to regularize subsequent mesh deformation. Note that the method proposed in [81], discussed in Section 3.2, for choosing R causes Σ_{local} and thus $\mathbf{n}_{\text{local}}$ (the third column of Σ_{local}) to vary inconsistently across the mesh. This can be remedied by constructing R more consistently from triangle to triangle, instead of using edge directions that vary significantly across the mesh. In order to do this, we use UV texture coordinates of the triangle vertices in order to reconstruct fairly consistent U and V directions across the mesh (see e.g. [59, Sec. 6.8]). Note that discontinuities in the texture coordinates can be ignored by removing neighbors from \mathcal{E} . Since U and V are not necessarily orthogonal, we retain U as our consistent direction and orthogonalize V to be perpendicular to U.

Boundary Displacements. Here, we consider $\mathbf{z}_i = \mathbf{x}_i^* - \mathbf{T}_i$, which is the distance from the outer boundary point \mathbf{x}_i^* of the Gaussian to the triangle centroid \mathbf{T}_i , in Eq. 9 in order to obtain $\mathcal{L}_{\text{reg}}^{\text{boundary}}$. This provides additional regularization (in addition to $\boldsymbol{\mu}_i - \mathbf{T}_i$) that constrains the shape of the Gaussians and more directly affects silhouette boundaries. Whereas [64] extracts boundary points using only a single Gaussian for each, we include the contribution from neighboring Gaussians in order to more accurately reflect the visible boundaries. In order to do this, we first define $\mathcal{N}(i)$ as a set that contains the Gaussian i itself along with its k -nearest neighbors in the UV texture space. Then, a ray is defined via $\mathbf{x}_i = \boldsymbol{\mu}_i + t\mathbf{n}_i$ where $\boldsymbol{\mu}_i$ is the center of the Gaussian, \mathbf{n}_i is the normal of the triangle the Gaussian is associated with, and t is the ray parameter. Next, for each Gaussian $j \in \mathcal{N}(i)$, we solve $\alpha_j G_j(\mathbf{x}_i) = \tau$ in order to find a boundary point of Gaussian j near Gaussian i based on the density threshold τ . Note that we do not consider Gaussians $j \in \mathcal{N}(i)$ that do not have $\alpha_j G_j(\boldsymbol{\mu}_i) < \tau$, which indicates that Gaussian j contains the center of Gaussian i based on the density threshold τ . Finally, \mathbf{x}_i^* is defined via t_i^* , where t_i^* is the maximum of the t_j found by solving $\alpha_j G_j(\mathbf{x}_i) = \tau$ for each $j \in \mathcal{N}(i)$.

4.2.2. Semantic Segmentation for Supervision

We train a segmentation model using the architecture from Mask2Former [18] with synthetic training data. Since MetaHuman textures are already semantically labeled, it is straightforward to generate synthetic training data in tex-

ture space. Moreover, since the labels are consistent from one MetaHuman to another, any manual adjustments to the labels only need to be done once. Fig. 4 (left) shows the labeled texture map with the neck, body, and hair all receiving the same (white) non-face label. The labeled images, Fig. 4 (middle), have an additional (black) label indicating the background region. In order to emphasize occlusion boundaries, the (black) background label is expanded to portions of the foreground to bound regions where the normals are becoming perpendicular to the view directions. This provides strong cues for the face silhouette.

Each Gaussian inherits a label from its associated triangle, and the triangle labels are derived from a template texture, Fig. 5 (left), that intentionally differs from Fig. 4 (left). Hairlines vary from person to person, and forcing triangles to align with an incorrect hairline can lead to spurious deformations of the forehead; thus, we expand the (red) face label in the template texture so that it includes regions that may or may not be covered with hair. It can be difficult to predict the boundary between the face and the neck, especially due to the non-linear deformations that occur in that region when someone turns their head; thus, we expand the face label in the template texture there as well. The remaining areas of the texture are given (black) background labels, in contrast to the (white) non-face foreground labels in Fig. 4 (left).

For each target image, the network from [73] is used to segment the foreground from the background; then, our segmentation network is used to predict foreground labels similar to Fig. 4 middle. Pixels with (white) non-face foreground labels are ignored during training, allowing Gaussians with any label to explain those regions of the image. In contrast, the (black) background labels are retained to emphasize occlusion boundaries. Let P be the set of pixels in the image that are not ignored and L be the number of labels (including



Figure 4. The annotated texture map (left) used to create training data: face (red), nose (blue), nostril (pink), top lip (green), bottom lip (cyan), eyes (yellow), ears (dark red), non-face (white). The labeled image (middle) has an additional (black) background label. Note how the (black) background label has been expanded to portions of the foreground in order to emphasize occlusion boundaries. The segmentation network is trained to recover Fig. 4 (middle) from Fig. 4 (right).

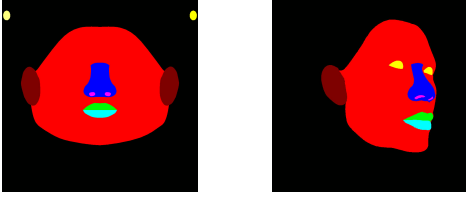


Figure 5. The template texture (left) used to assign labels to Gaussians: face (red), nose (blue), nostril (pink), top lip (green), bottom lip (cyan), eyes (yellow), ears (dark red), background (black). Note how the face label (red) has been expanded into both the hair and neck regions, as compared to Fig. 4. Note the differences between the labeled triangles (right) and what one would expect to obtain as image labels from the segmentation network (Fig. 4 middle).

the background) being used. Then, the segmentation loss is

$$\mathcal{L}_{\text{seg}} = \frac{1}{|P|} \sum_{p \in P} \left\| \hat{S}(p) - \text{onehot}_L(S(p)) \right\|^2 \quad (10)$$

where S is the segmentation label of pixel p and onehot_L converts from the set of segmentation labels to the set of basis functions $\{\mathbf{e}_1, \dots, \mathbf{e}_L\}$. \hat{S} is constructed using all visible Gaussians that overlap a pixel by alpha blending the one-hot encoding of their segmentation labels. \mathcal{L}_{seg} coerces Gaussians to explain the parts of the images that they belong to, which in turn will help to improve the alignment between the triangulated surface and the images (when the triangulated surface is later deformed, see Sec. 4.3).

4.2.3. Other Modifications

For each target image, the mesh is rendered from the current camera view in order to identify back-facing and occluded triangles, and Gaussians associated with those triangles are ignored with a certain probability. This makes Gaussians associated with visible triangles primarily responsible for explaining the target image. Note that the Gaussians associated with hidden triangles are not entirely discarded, since they may actually correspond to a portion of the target image. This allows them to drag their hidden triangles towards the appropriate portion of the target image.

An additional soft constraint is introduced to keep the eyeball and eye socket Gaussians from interfering with each other. Let x_{eyeball}^* and x_{socket}^* be the outer boundary points of the eyeball and eye socket Gaussians, respectively. For each eye socket Gaussian, let

$$\hat{x}_{\text{eyeball},i}^* = \arg \min_j \|x_{\text{eyeball},j}^* - x_{\text{socket},i}^*\|_2 \quad (11)$$

be the closest eyeball Gaussian, and let \mathbf{n}_i be the unit normal that points from the center of the eyeball (computed as the

mean of all $x_{\text{eyeball},j}^*$) to $\hat{x}_{\text{eyeball},i}^*$. Then,

$$\mathcal{L}_{\text{eyes}} = \frac{1}{N_s} \sum_{i=1}^{N_s} \left\| \max((\hat{x}_{\text{eyeball},i}^* - x_{\text{socket},i}^*) \cdot \mathbf{n}_i, 0) \right\|_2 \quad (12)$$

penalizes interference between the eyeball and eye socket Gaussians. N_s is the number of Gaussians representing the eye socket. See Fig. 6.

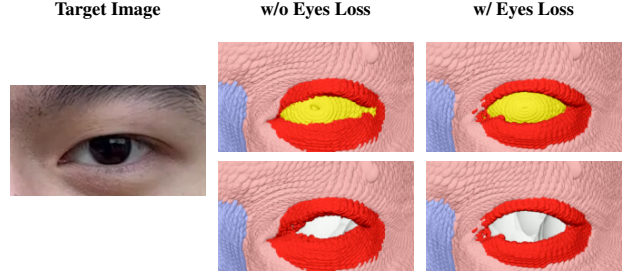


Figure 6. The results obtained without and with the eye regularization loss ($\mathcal{L}_{\text{eyes}}$ in Eq. 12), respectively. The top row shows all the Gaussians, while the bottom row omits the (yellow) eyeball Gaussians in order to more clearly illustrate the errors in the (red) eye socket Gaussians. Although both variations match the target image, the result obtained without $\mathcal{L}_{\text{eyes}}$ achieves this by allowing the eyeball Gaussians to occlude the eye socket Gaussians. The resulting mesh would have an inaccurately small eye socket. This is alleviated by $\mathcal{L}_{\text{eyes}}$.

4.3. Triangulated Surface Deformation

We use our modified Gaussian Splatting to jointly optimize the camera extrinsics and Gaussian parameters, as is typical. Afterwards, the camera extrinsics are held fixed during geometry refinement. Each iteration, the Gaussian parameters are re-optimized in order to provide supervisory information for subsequent deformation of the triangulated surface. The supervisory information takes the form of outer boundary points for each Gaussian, i.e. the \mathbf{x}_i^* from Sec. 4.2.1, except that the combined contribution (replacing the max in Sec. 4.2.1 with a sum) of each Gaussian and its k -nearest neighbors is used. That is, for each Gaussian i ,

$$\sum_{j \in \mathcal{N}(i)} \alpha_j G_j(\boldsymbol{\mu}_i + t_i^* \mathbf{n}_i) = \tau \quad (13)$$

is solved to find a ray parameter t_i^* that defines the outer boundary point $\mathbf{x}_i^* = \boldsymbol{\mu}_i + t_i^* \mathbf{n}_i$.

The vertices \mathbf{v} of the triangulated surface are perturbed by minimizing

$$\mathcal{L}_{\text{centroid}} = \sum_i \left\| \mathbf{v}_i^{\text{centroid}} - \mathbf{x}_i^* \right\|^2 \quad (14)$$

where the triangle centroid $\mathbf{v}_i^{\text{centroid}}$ is the average of the triangle vertices. In addition to the data term in Eq. 14, two regularization terms are also included in the minimization. $\mathcal{L}_{\text{reg}}^{\text{vertex}}$ aims to keep the perturbation of each vertex equal to average perturbation of its edge-connected neighbors, and $\mathcal{L}_{\text{reg}}^{\text{normal}}$ penalizes the difference between changes in the normal direction. Additional regularization can be had by optimizing over the coefficients of a PCA basis, instead of optimizing over the individual vertex positions directly. We perform two iterations of geometry refinement, using a MetaHuman per-region PCA formulation [33] in the first iteration and individual vertex positions in the second. As mentioned above, the Gaussians parameters are re-optimized (using the current best guess for the geometry) before each of these iterations.

4.4. Neural Texture Approach

Although Gaussian Splatting approaches typically use a triangulated surface that only roughly approximate the geometry, we illustrate the benefits of having an accurately reconstructed triangulated surface in the section. Importantly, this accurately reconstructed triangulated surface is valuable even when one prefers the look of Gaussian Splatting to that which can be obtained via a standard graphics pipeline utilizing textured triangles. This emphasizes the efficacy of our contribution. Although neural approaches have become quite popular in the literature, they have not been widely adopted in industry. It took decades to develop the software and hardware used in the modern graphics pipeline, and the various development were shaped by the need to embrace artist creativity and control in every aspect of the pipeline. Thus, less invasive approaches are likely to facilitate quicker industry adoption. In this vein, we propose moving the Gaussian Splatting model out of world space and into texture space. This retains all the conveniences and efficiencies of the software and hardware graphics pipeline while still using Gaussian Splatting on assets of interest via a view-dependent neural texture. Of course, neural textures require more accurate geometry, again emphasizing the efficacy of our contribution.

It is straightforward to transform world space triangles to texture space, since their vertices already have UV coordinates. The resulting transforms can be used to move the Gaussians into a 3D UVW texture space in the same manner that the Gaussians are moved from canonical space to world space (see Sec. 3.2). Note that W encodes the orthogonal distance from each Gaussian to its parent triangle. A view-dependent neural texture can then be computed by splatting the Gaussians perpendicularly with an “orthographic camera” while still defining their color as a function of the world space camera view as usual. Since the Gaussians live in a canonical space, it is straightforward to compute both their world space and texture space locations. Although there are

an infinite number of ways to represent a view-dependent neural texture, we argue that the Gaussians provide an exceptionally good basis, as evidenced by their efficacy in providing world space structure to camera space images.

Rendering the triangulated surface with a simple ambient-only shader allows for a straightforward comparison between standard Gaussian Splatting (Fig. 7, first image) and our newly proposed neural texture approach (Fig. 7, second image). Notably, the neural texture computes the color at each point on the triangulated surface by α -blending Gaussians along the normal direction instead of the usual approach of α -blending along the ray direction. See Fig. 8. In addition, pixels that overlap Gaussians but do not overlap the triangulated surface are not shaded at all. Both of these differences emphasize the need for the accurate geometry provided by our method.

Since the Gaussians are being used differently, it makes sense to retrain them (using their current parameters as a warm start). After fine-tuning, the model generates even cleaner details (Fig. 7, third image) than the standard approach (Fig. 7, first image). For the sake of computation efficiency, we also experimented with replacing the usual α -blending with a direct summation (along the lines of [119]). This allows for purely 2D Gaussians in UV space (Fig. 7, fourth image).

Treating the Gaussians as a neural texture has other advantages as well. For example, a mipmap can be created by reducing both the number of texels and the number of Gaussians. Notably, it is quite straightforward to accomplish this in texture space in contrast to the difficulties associated with significantly reducing the number of Gaussians for level of detail representations in world space.

Importantly, Gaussian Splatting does a good job dealing with camera extrinsics, allowing for the creation of an accurate triangulated surface geometry. However, after asset creation, it seems that Gaussian Splatting can be replaced with a simpler neural or even spherical harmonic texture with no loss of efficacy.

4.5. Lighting Estimation

Spherical harmonics [82] is used to approximate the lighting conditions via $\sum_k l_k A_k Y_k(\mathbf{n}_p)$, where \mathbf{n}_p is a per-pixel unit-length surface normal, Y_k are diffuse spherical harmonic basis functions, A_k are normalization constants, and the l_k are learned three-color-channel coefficients. In order to encourage uniform values across color channels to prevent color overfitting, the zeroth order coefficients are regularized via $\mathcal{L}_{\text{lighting}} = \|\mathbf{l}_0 - \bar{\mathbf{l}}_0\|_2$, where $\bar{\mathbf{l}}_0$ is the mean value across the three color channels. Each \mathbf{n}_p is computed by perturbing the interpolated vertex averaged normal by a learned per-pixel rotation R_p meant to mimic a normal map. Each Gaussian is given an additional learnable parameter R_i , and the R_i are alpha-blended (as usual) in order to determine per-



Figure 7. A comparison of standard Gaussian Splatting (first image) to a view-dependent neural texture (other three images) for a novel view. The second image shows the results obtained by using parent triangles to transform the Gaussians into UVW texture space, and the third image shows the results obtained after fine-tuning those transformed Gaussians using the original views (this novel view is not used for the fine-tuning). The fourth image removes the α -blending by replacing it with a direct summation, so that the Gaussians can be defined in a 2D UV texture space instead of a 3D UVW texture space for the sake of efficiency (if desired). For the sake of comparison, all the images still utilize world-space Gaussians for the non-face (hair, neck, eyeballs, etc.) regions.

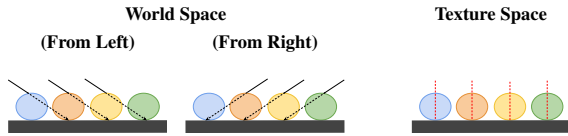


Figure 8. In the world space approach, color accumulation is performed along the ray direction; thus, the mixing of Gaussians is view-dependent. When viewed from the left, Gaussians to the left of each point on the surface need to properly combine with the Gaussians above those points. When viewed from the right, Gaussians to the right of each point on the surface need to properly combine with the Gaussians above those points. In contrast, the texture space approach always accumulates in the same direction, orthogonal to the texture, regardless of the view direction. This helps to prevent the blurriness issue for novel views, where the Gaussians are accumulated in ways that were unanticipated during training. In addition, reducing the influence of neighboring Gaussians increases the locality and compactness of the texture space approach (as compared to the world space approach) creating a smaller circle of confusion and thus intrinsically higher resolution.

pixel R_p . Regularization of the form $\mathcal{L}_{\text{rotation}} = \|R_p - I\|_F^2$ is added to limit the magnitude of the rotation. This normal map reduces color artifacts around fine-scale features such as wrinkles.

To improve rendering quality near occlusion boundaries and reduce baked-in shadows, we precompute a screen-space occlusion map for each target image, similar to [46]. For each pixel, the corresponding point x_p on the triangulated surface is identified; then, Monte Carlo integration over the hemisphere centered about (x_p, n_p) is used to compute a

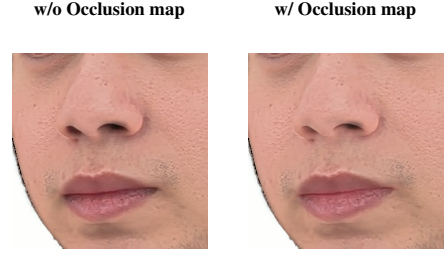


Figure 9. De-lit images recovered without and with the occlusion map, respectively. The occlusion map reduces baked-in ambient shadows, particularly in recessed regions such as below the nose and along the lip crease, improving the de-lit textures.

per-channel visibility fraction

$$f_{\text{visible}}(p; l) = \frac{\sum_k l_k \sum_j V(x_p, d_j) Y_k(d_j) n_p \cdot d_j}{\sum_k l_k \sum_j Y_k(d_j) n_p \cdot d_j} \quad (15)$$

where the visibility in direction d_j , i.e. $V(x_p, d_j) \in \{0, 1\}$, is computed based on the mesh geometry. Since f_{visible} is expensive to evaluate, it is only computed occasionally using the current best guess for n_p and the l_k . Denoting the lagged l_k as l_{visible} , the per-pixel per-channel lighting estimate is given by

$$L(p; l, l_{\text{visible}}) = f_{\text{visible}}(p; l_{\text{visible}}) \sum_k l_k A_k Y_k(n_p) \quad (16)$$

where n_p depends on both the triangulated surface and the learned normal map. See Fig. 9.

4.6. De-lit Texture Generation

Although our method is motivated by [87], their method relies on a large light stage dataset and thus cannot be applied directly to our limited number of images taken by a single camera without known or constrained lighting. To address this, we regularize the problem with a rendering of the reconstructed triangulated surface using the low-dimensional texture space available in the MetaHuman framework; in particular, we use the first 20 (out of a total of 137) PCA coefficients. This leads to a texture $\sum_j c_j T_j$ where the T_j are three-channel PCA basis functions and the c_j are learned during training. Augmenting this regularized texture with Gaussian Splatting allows the model to match the training data. The goal is to limit the contribution of the Gaussians to high-frequency texture details and lighting variations in order to obtain a de-lit mesh-based texture. See Fig. 10 for an overview of our approach.

For each pixel, the per-pixel lighting estimate (see Sec. 4.5) is multiplied channel-by-channel by the triangulated surface texture interpolated to that pixel. A per-pixel compositing weight β_p is used to combine the contribution from the Gaussians with a $1 - \beta_p$ contribution from the

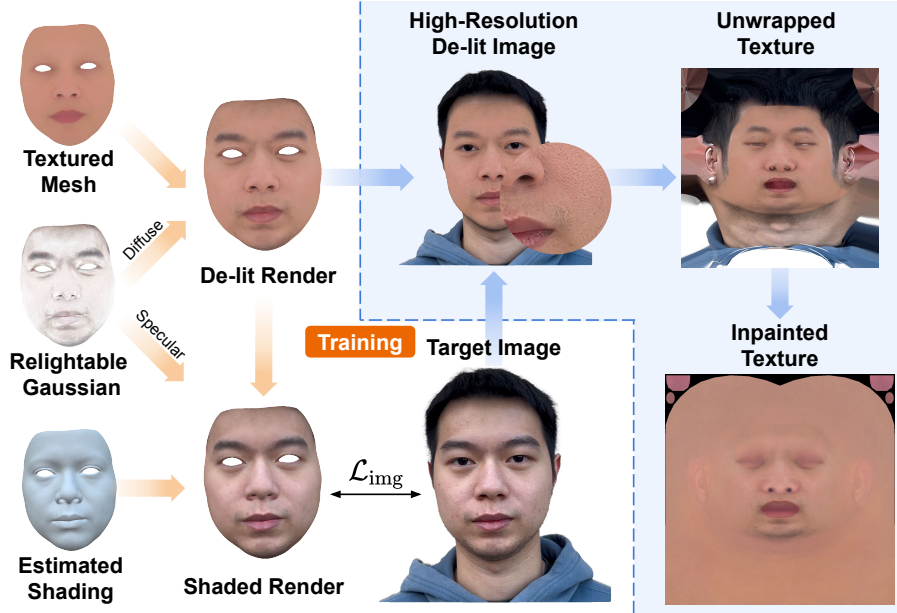


Figure 10. Our method combines a textured mesh with a relightable Gaussian model and estimated spherical-harmonics lighting to reproduce a target image. After training, we render the view-independent albedo component to obtain a de-lit image and reintroduce high-frequency details extracted from the reference image. The resulting high-resolution de-lit images are then unwrapped and inpainted to form a complete high-resolution de-lit texture.

triangulated surface. Each Gaussian is given an additional learnable parameter β_i , and the β_i are alpha-blended (as usual) in order to determine per-pixel β_p . During training, the β_i are regularized toward zero via $\mathcal{L}_{blending} = \|\beta_p\|_2$ in order to favor reliance on the mesh.

For the Gaussian model, we modify the method proposed in Sec. 3.3 in a number of ways in order to provide regularization aimed to compensate for our much more limited access to data. The diffuse term in Eq. 7 is calculated by alpha compositing the learned albedo ρ along the lines of Eq. 3 before multiplying it by the per-pixel lighting estimate (from Eq. 16). The specular term in Eq. 8 and simplifications thereof seem intractable in the face of limited data; thus, we replace Eq. 8 with an extra view-dependent color term c , identical to that which was discussed in and after Eq. 3. That is, motivated by [87], we augment [53] to include an extra view-independent diffuse term evaluated with the aid of a spherical harmonic lighting estimate. The intent is to have this diffuse term explain as much of the lighting as possible, so that the original view-dependent color term can be minimized via $\mathcal{L}_{view} = \|c\|_2$.

After training, de-lit images can be obtained by ignoring the view-dependent color term and by setting the per-pixel lighting estimate equal to a value of one. Lost or damaged high-frequency texture details can be restored by extracting them from the target images (via a high-pass filter) and using them to replace the equivalent high-frequency content in the de-lit images. Note that the target images are warped to bet-

ter align with the triangulated surface geometry (see [126]) before the high-frequency content is extracted. The method proposed in [67] is used to project the corrected de-lit image data into texture space where it can be gathered to texels in order to obtain a de-lit texture.

Although using [67] to project and gather a de-lit texture results in a high-quality result for most of the face, there are some problematic areas. The eyebrows and other hair regions will have artifacts baked into the texture, the neck region suffers from limited visibility, the hairline on the scalp will be erratic, etc. We remedy these issues by creating a mask in texture space that separates the high-quality results from the regions that are typically problematic. The texture in the high-quality region is projected into the MetaHuman texture space to find PCA coefficients for a global texture that can be used to inpaint the problematic regions; afterwards, blending is used to soften the texture transition at region boundaries.

4.7. MetaHuman Generation

Although we started with an initial guess that was consistent with the MetaHuman framework (see Section 4.1), the geometry perturbations discussed in Section 4.3 lead to a vertex layout (sometimes referred to as spans in the industry) that is inconsistent with the underlying MetaHuman basis. Thus, we use the mesh-to-MetaHuman [32] tool to convert our reconstructed geometry back into the MetaHuman basis. Since this process perturbs vertex positions, the PCA basis function used for the texture no longer correspond to the

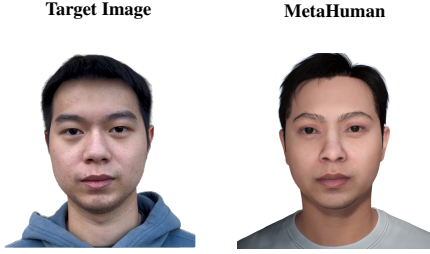


Figure 11. Target image (left) and the MetaHuman reconstructed with our pipeline (right). Note that the hair style, eyebrow style, and eyeballs are manually selected from the MetaHuman database.

same surface locations. We remedy this by repeating the lighting estimate and texture solve (discussed in Section 4.5 and Section 4.6) on the new geometry. Obviously, it would be more efficient if only one lighting and texture solve were required; however, the mesh-to-MetaHuman process requires an input texture (and better textures give better results). Although the teeth, inner mouth, and eyelashes are added back to the geometry via the mesh-to-MetaHuman process, we ignore them (as usual) during the lighting estimate and texture solve. Alternatively, MetaHuman Creator [31] in Unreal Engine 5.6, can be used to better preserve the input geometry; in addition, this alleviates the need to repeat the lighting and texture solve. See Fig. 11

5. Implementation Details

Follow [120], we combine a standard per-pixel \mathcal{L}_1 loss with a structural similarity loss (SSIM from [106]), i.e.

$$\mathcal{L}_{\text{img}} = (1 - \lambda)\mathcal{L}_1 + \lambda\mathcal{L}_{\text{D-SSIM}} \quad (17)$$

where $\mathcal{L}_{\text{D-SSIM}}$ multiplies the structural similarity by negative one so that it is maximized, and $\lambda = 0.2$. This approach is also followed by [53, 81]. \mathcal{L}_{img} is used in every stage of the Gaussian training. In both the camera and geometry optimization passes, the regularization terms discussed in Sec. 4.2.1 are included; in addition, $\lambda_{\text{scale}} = 50$ for $\mathcal{L}_{\text{scale}}$ from Sec. 3.2. In the camera optimization pass, $\lambda_{\text{reg}}^{\text{center}} = 10$, $\lambda_{\text{reg}}^{\text{normal}} = 10$, and $\lambda_{\text{reg}}^{\text{boundary}} = 50$. In the geometry optimization pass, $\lambda_{\text{reg}}^{\text{center}} = 20$, $\lambda_{\text{reg}}^{\text{normal}} = 10$, $\lambda_{\text{reg}}^{\text{boundary}} = 500$. In both passes, $\lambda_{\text{seg}} = 50$ for \mathcal{L}_{seg} from Sec. 4.2.2, and $\lambda_{\text{eyes}} = 20$ for $\mathcal{L}_{\text{eyes}}$ from Sec. 4.2.3. During texture reconstruction, the regularization terms from Sec. 4.5 and Sec. 4.6 use $\lambda^{\text{lighting}} = 10^{-3}$, $\lambda^{\text{rotation}} = 0.2$, $\lambda^{\text{blending}} = 0.1$, and $\lambda^{\text{view}} = 10^{-3}$.

The model is trained for 5000 iterations with one Gaussian per triangle in both the camera and geometry optimization passes. Before texture reconstruction, the mesh is subdivided (without perturbing vertex positions) and each Gaussian is split into four Gaussians. The new Gaussians are

located at the centers of the sub-triangles and otherwise inherit the properties of their parent Gaussian, except for a reduction in scale by a factor of two. An additional 1000 iterations are used to refine the densified model. During texture reconstruction, opacity, position, rotation, and scale are kept fixed, and the learnable parameters are initialized as follows: albedo and the view-dependent spherical harmonic coefficients are set randomly, compositing weights are set to 0.05, and normal map rotations start at the identity. The texture reconstruction model is trained for 2000 iterations.

We use a learning rate of 5×10^{-3} for all Gaussian parameters, except for scale and compositing weights which use 1×10^{-3} and 2×10^{-2} respectively. Slowing the convergence of scale allows the model to better benefit from the segmentation supervision. In the camera optimization pass, the learning rate for camera extrinsics is set to 1×10^{-2} . During texture reconstruction, the learning rate for the lighting estimates is set to 5×10^{-4} and the learning rate for the mesh-based texture PCA coefficients is set to 1×10^{-2} . We followed the training protocol of [81] for all other implementation details not explicitly specified.

When perturbing the vertices of the triangulated surface as discussed in Sec. 4.3, we optimize the parameters (either PCA coefficients or vertex positions) for 2000 iterations using Adam [55] with a learning rate of 5×10^{-3} . $\mathcal{L}_{\text{centroid}}$ is combined with the regularization terms via $\lambda_{\text{reg}}^{\text{vertex}} = 2$ and $\lambda_{\text{reg}}^{\text{normal}} = 0.2$. In the PCA optimization, we found it useful to penalize coefficients that exceeded a value of 1 via $\lambda_{\text{reg}}^{\text{PCA}} = 1$.

5.1. Segmentation Model Training

The segmentation network, described in Sec. 4.2.2, was trained on 1600 randomly sampled identities from the MetaHuman Creator [31]. Five 720×720 resolution images were used for each identity, yielding 8000 total image pairs (Fig. 4, middle and right). Random eye controls, including blinking, were included in the otherwise neutral facial expressions. Lighting conditions were randomly sampled from the 11 available environment presets. The 25° FoV camera always pointed at the center of the head, and its distance from the center of the head was varied randomly from 45 to 80 cm. Measured from the horizontal ray through the center of the head that extends through the front middle of the face, the pitch and yaw were randomly sampled to be between $\pm 40^\circ$ and $\pm 80^\circ$, respectively. We trained the model for 40,000 iterations with a batch size of 4, and all other training details follow the default settings of [18, 22]. An additional 60 randomly sampled identities, yielding 300 total image pairs, were used for validation.

6. Experiments

For each in-the-wild reconstruction, we capture monocular video data as discussed in Sec. 4.1; then, eleven predefined

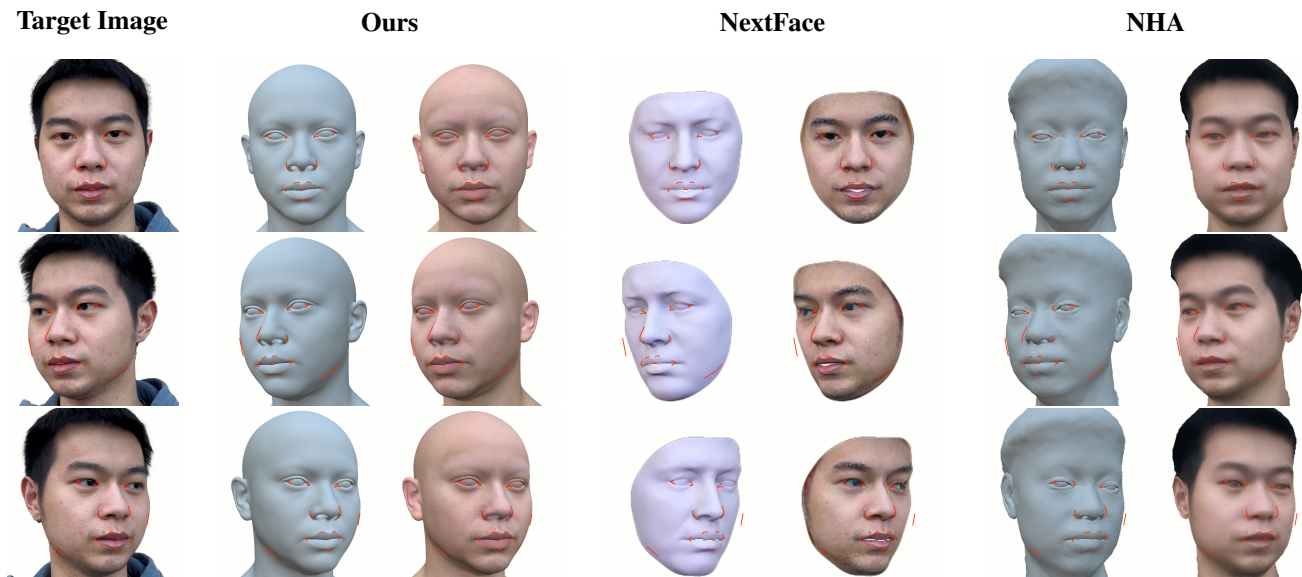


Figure 12. Geometry reconstruction results comparing our method to NextFace [28] and NHA [42]. Contour curves have been overlaid on key facial features in order to facilitate comparisons. Comparing column 2 to columns 4 and 6 illustrates that our method reconstructs better geometry. It is important to stress that the projection of colors (overfit to an image) onto geometry, as shown in columns 5 and 7, obfuscates errors in geometry reconstruction.

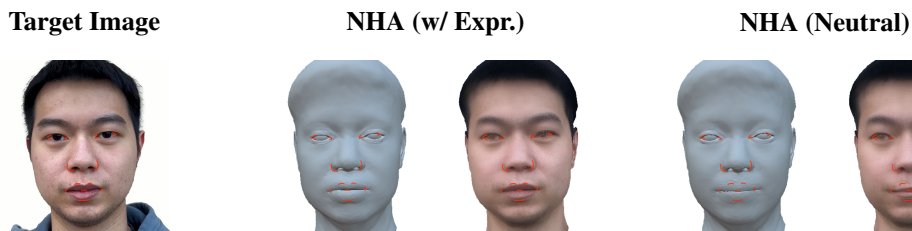


Figure 13. Allowing NHA [42] to overfit expressions to the target images does give slightly better results than those that are obtained by fixing the expression to be held in a neutral pose, as we did for Fig. 12 (compare the 2nd and 3rd images here to the top right of Fig. 12). However, as is typical, this expression overfitting leads to a poor (unusable) neutral pose as shown in the last two images.

target head poses are chosen for the reconstruction.

We ran various ablation tests to evaluate the efficacy of our contributions. Omitting our segmentation supervision causes Gaussians to be assigned to incorrect semantic regions, i.e., sliding from nearby regions (e.g. the lip region) or originating from different layers when Gaussians overlap (e.g. the eye region). Omitting our soft constraints disconnects the Gaussian explanation from their triangles causing the Gaussians to become disorganized with large size and shape variations. In both cases, the quality of the reconstructed mesh is deteriorated. See Fig. 2. Ablation test for the eye regularization loss and occlusion map are shown in Fig. 6 and Fig. 9, respectively.

6.1. Comparison with Prior Work

Fig. 12 compares our method with NHA [42] and NextFace [28]. For [28], we use the multi-image version

for their reconstruction. For [42], we set their expression and jaw pose coefficients to neutral and set their camera intrinsics to match ours; otherwise, their method overfits to obtain an unusable neutral expression (see Fig. 13). Both of these state-of-the-art approaches exhibit misalignment of semantic facial regions and (especially [28]) fail to capture the facial silhouette in side views. Lacking a strong semantic correspondence between their reconstructed geometry and the image data, many methods allow texture to slide on the geometry as it overfits to the image. This obfuscates errors in geometry reconstruction, not only from those who intend to use the method, but also from the method itself. That is, methods that allow for texture sliding hinder their own ability to improve the geometry, since the final result no longer differs from the image data. Our semantic segmentation and soft constraints have been devised specifically to address this issue. Since [28] and [42] do not obtain high quality de-

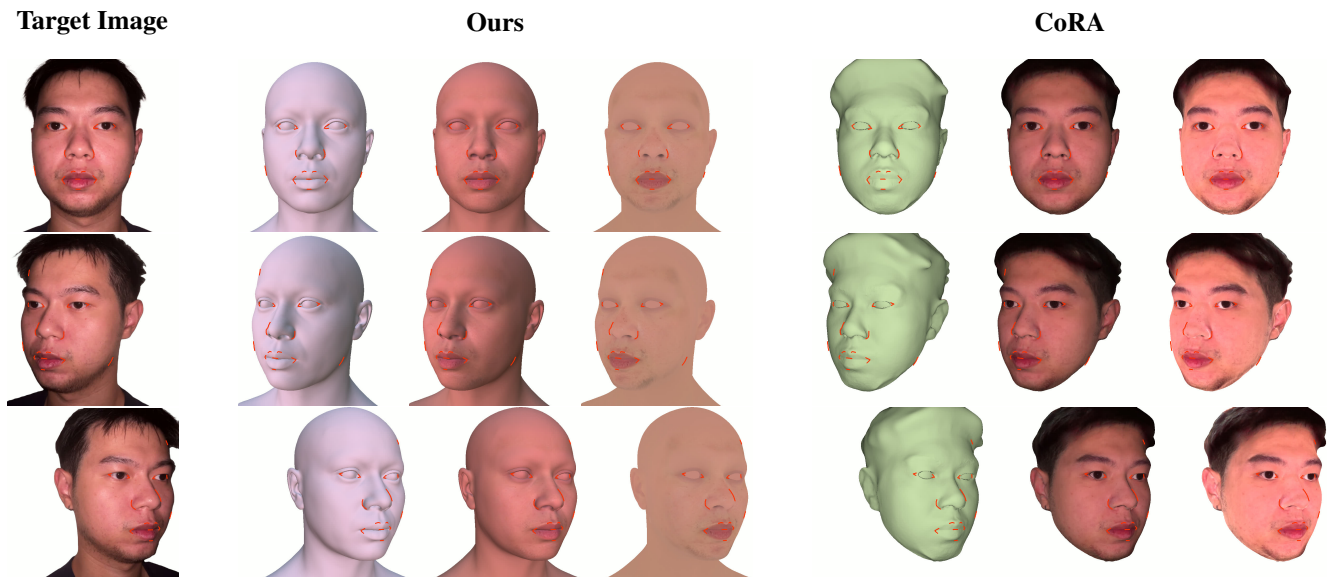


Figure 14. Comparison between our method and CoRA [44], using their proposed method for data capture. Contour curves have been overlaid on key facial features in order to facilitate comparisons. Comparing column 2 to column 5 illustrates that our method reconstructs better geometry. CoRA introduces artifacts around the nose and jaw regions. These artifacts are also evident in the de-lit texture (column 7). Comparing column 4 to column 7 illustrates that CoRA has more baked-in lighting in their textures. This makes them incorrectly appear more three-dimensional, rather than flat (a de-lit texture should appear flat, see Fig. 15). Columns 3 and 6 show the de-lit textures from columns 4 and 7 combined with the estimated lighting, in order to compare with the target image.

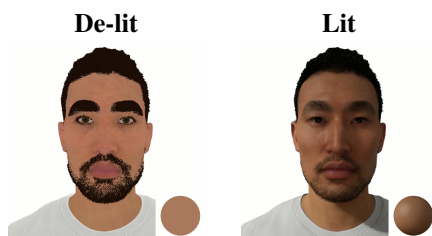


Figure 15. Left: Ambient-only lighting on both a MetaHuman and a sphere. Right: Full lighting on both. Note how flat the de-lit version appears to be, turning a three-dimensional sphere into a flat two-dimensional circle.

lit textures, we instead compare our texture reconstruction approach to other methods.

Fig. 14 compares our method with the approach proposed in [44], which uses flashlight capture to obtain image data. Following their instructions, we obtained similar data for our subject. The results labeled “CoRA” in the figure use their approach on this data, and the results labeled “Ours” in the figure use our approach on a subset of the data (our approach requires only 11 frames, see Fig. 3). The artifacts around the lips, nose, and jaw in the CoRA result are primarily due to an incorrect disentanglement of geometry and texture that allows errors in albedo and surface normals to offset each other; however, note that CoRA does achieve much better disentanglement than [28] and [42]. In compar-

son to CoRA, our method recovers sharper boundaries for facial features. This is especially important because their results are not readily animatable (ours are), meaning that further errors will result when converting their soft implicit surface boundaries to an explicit mesh that can be rigged for animation. Importantly, our method achieves similar de-lit textures under various lighting conditions (see Fig. 16). This consistency foreshadows how well our de-lit texture can be re-lit under novel lighting conditions, as shown in Fig. 17.

6.2. Utilizing Disparate Captures

Our method is flexible enough to utilize images captured with disparate setups and lighting conditions. For example, we can combine images from our outdoor capture (see Sec. 4.1) with images acquired using flashlight illumination (see e.g. [44]). Despite the differences, our approach is able to successfully integrate both datasets in order to produce a consistent geometry. Leveraging heterogeneous inputs facilitates the removal of spurious geometric variations, regularizing away slightly non-neutral facial expressions, small eye-shape differences, imperfections in camera intrinsics/extrinsics, etc. This is readily accomplished by allowing each Gaussian to maintain a separate view-dependent color for each disparate batch of images, while sharing all other attributes (opacity, position, scale, rotation, segmentation label, etc.). Importantly, our segmentation supervision provides reliable geometric cues, preventing the per-capture view-

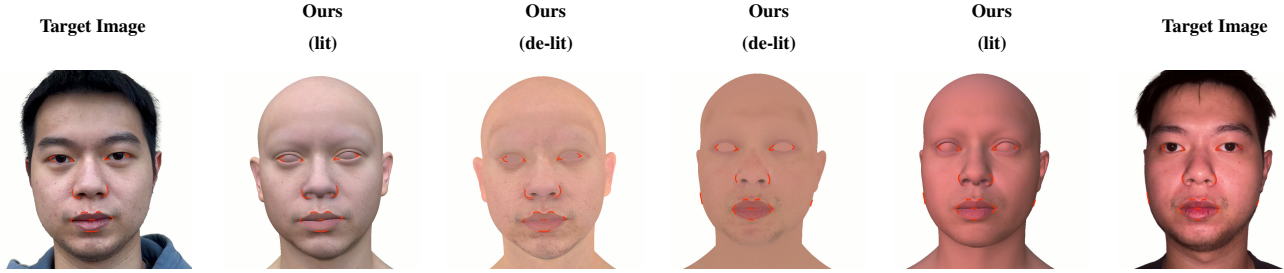


Figure 16. Note how similar our de-lit textures appear (compare columns 3 and 4), despite the disparate lighting in the two tests. Also note how well our de-lit textures respond to the lighting (columns 2 and 5), allowing for good matching to the target images (columns 1 and 6).

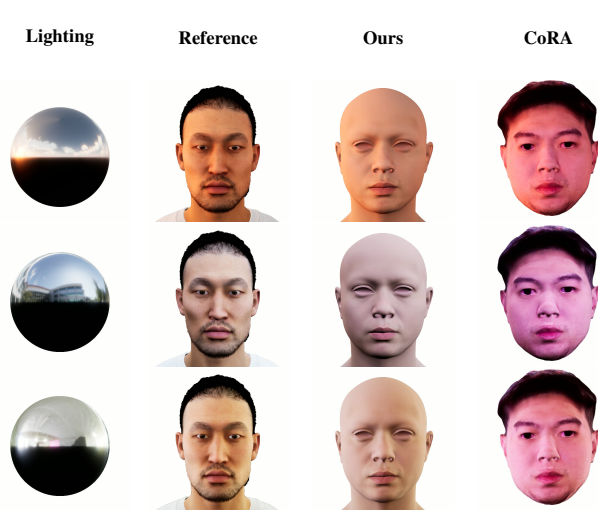


Figure 17. Each row illustrates a novel lighting condition, depicted by a chrome sphere (column 1) and the rendering of an artist-created MetaHuman (column 2). Our reconstructed texture (column 3) matches the reference quite well, especially when compared to CoRA (column 4).

dependent color from overfitting. When one batch of images is deemed more reliable, its influence can be increased by sampling from it more often during training. In fact, only the most reliable images should be used for the texture reconstruction, as regularization aims to blur important features. See Fig. 18.

6.3. Text-driven Asset Creation

We demonstrate the efficacy of our approach by integrating it into a text-driven asset creation pipeline. First, we use ChatGPT [77] to generate an image with a neutral expression. Then, we use Veo 3 [25] to create a video from the image using the instruction “The actor rotates their head around.” This creates data similar to our capture setup. Afterwards, our pipeline can be executed as usual. See Fig. 19.

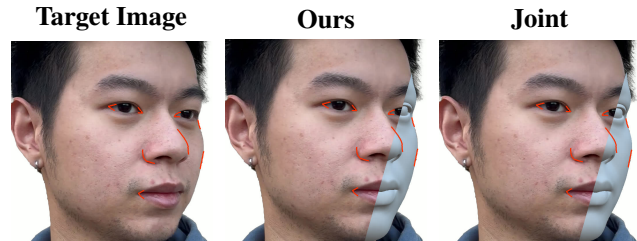


Figure 18. The middle image shows the result obtained using (only) our data capture strategy, while the far right image shows the result obtained when combining our data with the data obtained via flashlight capture. The additional flashlight capture data improves rigid alignment, particularly in side views, as can be seen from the better aligned eye and lip contours.



Figure 19. The reference image (left) was generated via a ChatGPT prompt, and it was subsequently used to create a video via Veo 3. The top row shows selected images from the video, and the bottom row shows the result of our pipeline.

6.4. Additional Results

We provide reconstruction results for the identity shown in Fig. 12 from additional views in Fig. 21., and results for an additional identity in Fig. 20.

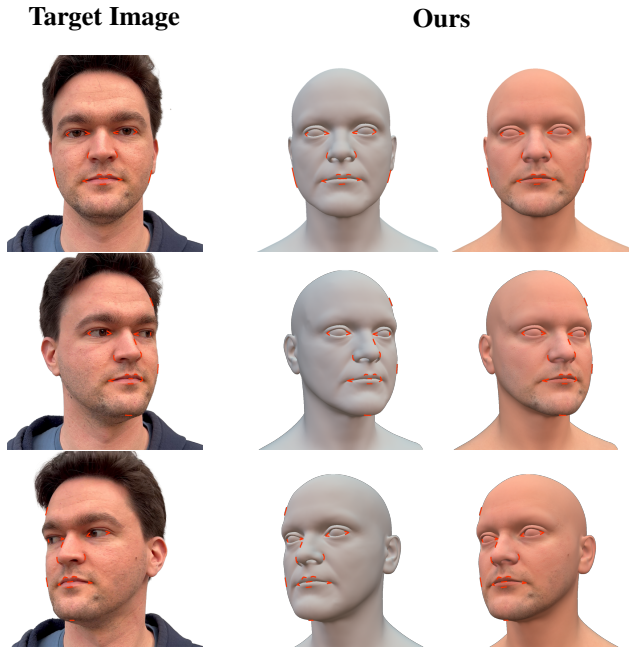


Figure 20. Reconstruction results for an additional identity.

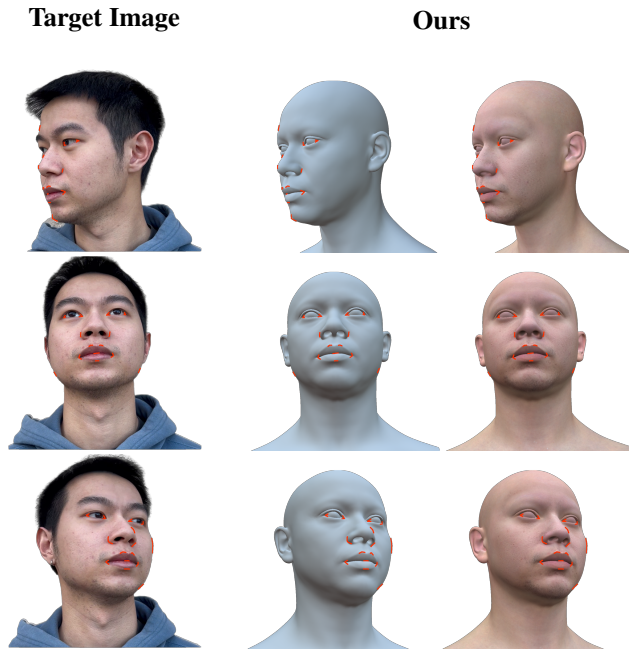


Figure 21. Reconstruction results of the identity shown in Fig. 12 from additional views.

7. Limitations

In spite of the progress we have made addressing de-lighting, it remains difficult to address without a light-stage or similarly non-democratizable specialized equipment. Our de-

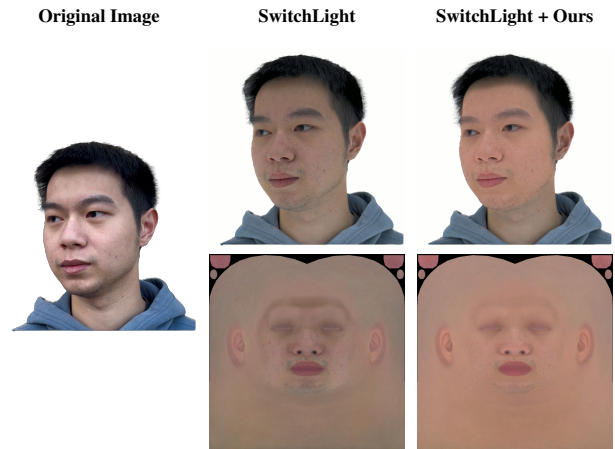


Figure 22. Column 1 shows the results obtained using SwitchLight [54] to preprocess the images before using [67] to project and gather a texture. Note that the eyebrows, neck, hairline etc. have been inpainted via the PCA-based projection approach discussed at the end of Sec. 4.6. Column 2 shows the result obtained using SwitchLight to preprocess the images before fitting them into our pipeline. Although SwitchLight does a reasonable job, our method further suppresses baked-in shadows and aligns the texture with the MetaHuman color space (e.g. the SwitchLight result is too dark).

lighting approach sacrifices some fine-grained geometric details, such as wrinkles. Although surface normal information could help to address this, Gaussians are not yet able to predict surface normals accurately enough to provide a remedy.

The eyes and eyelids are the most difficult regions for our method to properly capture. This is because the overlapping Gaussians used in these regions do not have precise segmentation or strong silhouette guidance. While semantic segmentation does provide some supervision, it operates at a coarse granularity. Improvements could be achieved by incorporating high-quality, fine-grained landmark prediction.

Our framework focuses primarily on the face and does not extract or regularize geometry for the hair, neck, etc. See e.g. [52, 102, 117] for various options/discussions. Gaussians in these areas remain unstructured and are thus not used to optimize the geometry of the triangulated surface. This may make camera pose estimation less reliable and sometimes cause the reconstructed geometry to deviate from the true head shape.

8. Conclusion

Our method leverages the remarkable ability of Gaussian Splatting to explain a set of disparate images in a cohesive way with a disentangled view, essentially solving the camera extrinsics problem for democratizable approaches. Our modifications of Gaussian Splatting facilitate its use in geom-

etry reconstruction. The semantic segmentation supervision allows the Gaussians to create accurate correspondences between the image and the triangulated surface. The soft constraints provide regularization and structure to the correspondence. Our geometry reconstructions compare favorably to the state-of-the-art. For texture, leveraging a PCA-based albedo prior and a Relightable Gaussian Splatting model allowed us to disentangle illumination from reflectance. This resulted in a cleaner, flatter, and more consistent de-lit texture than that which could be obtained by other democratizable methods not relying on controlled lighting or a light stage. Together, these design choices yield an accurate, relightable, and animatable reconstruction that generalizes well across subjects and lighting conditions, while remaining fully compatible with standard graphics pipelines.

Our approach is flexible enough to be used on a wide range of data sources and capture setups, readily accommodates disparate data, and can leverage inputs from other approaches. Notably, our ability to utilize disparate image data facilitates the hybridization of our approach with portrait-editing approaches (see e.g. [16, 72, 84]). In particular, [54] achieves impressive portrait de-lighting and can be used to de-light images before they are used in our pipeline. See Fig. 22.

Even in the case where Gaussian Splatting is preferred over the geometry and texture of a standard graphics pipeline, obtaining good geometry (as our method enables) is still rather useful. For example, better geometry provides better accuracy when driving Gaussian Splats during animation. Accurate geometry also allows, as shown in Sec. 4.4, the Gaussian Splats to be transformed into texture space where they can be used as a view-dependent neural texture. This allows any asset (or any subset of any asset) to be treated with Gaussian Splats without the need to modify any other assets or any other aspect of the graphics pipeline, facilitating immediate use of Gaussian Splats in high-end applications.

9. Acknowledgement

Research supported in part by ONR N00014-24-1-2644, ONR N00014-21-1-2771, and ONR N00014-19-1-2285. We would like to acknowledge Epic Games for additional support.

References

[1] Ashutosh Agarwal and Chetan Arora. Attention attention everywhere: Monocular depth prediction with skip attention. In *Proceedings of the IEEE/CVF Winter Conference on Applications of Computer Vision (WACV)*, pages 5861–5870, 2023. 5

[2] ShahRukh Athar, Zhixin Shu, and Dimitris Samaras. Flame-in-nerf: Neural control of radiance fields for free view face animation. In *2023 IEEE 17th International Conference on*

Automatic Face and Gesture Recognition (FG), pages 1–8. IEEE, 2023. 3

[3] Andrew D Bagdanov, Alberto Del Bimbo, and Iacopo Masi. The florence 2d/3d hybrid face dataset. In *Proceedings of the 2011 joint ACM workshop on Human gesture and behavior understanding*, pages 79–80, 2011. 3

[4] Haoran Bai, Di Kang, Haoxian Zhang, Jinshan Pan, and Linchao Bao. Ffhq-uv: Normalized facial uv-texture dataset for 3d face reconstruction. In *Proceedings of the IEEE/CVF conference on computer vision and pattern recognition*, pages 362–371, 2023. 3

[5] Ziqian Bai, Feitong Tan, Zeng Huang, Kripasindhu Sarkar, Danhang Tang, Di Qiu, Abhimitra Meka, Ruofei Du, Mingsong Dou, Sergio Orts-Escolano, et al. Learning personalized high quality volumetric head avatars from monocular rgb videos. In *Proceedings of the IEEE/CVF Conference on Computer Vision and Pattern Recognition*, pages 16890–16900, 2023. 3

[6] Linchao Bao, Xiangkai Lin, Yajing Chen, Haoxian Zhang, Sheng Wang, Xuefei Zhe, Di Kang, Haozhi Huang, Xinwei Jiang, Jue Wang, et al. High-fidelity 3d digital human head creation from rgb-d selfies. *ACM Transactions on Graphics (TOG)*, 41(1):1–21, 2021. 3, 4

[7] Volker Blanz and Thomas Vetter. A morphable model for the synthesis of 3d faces. In *Seminal Graphics Papers: Pushing the Boundaries, Volume 2*, pages 157–164. 2023. 3

[8] James F Blinn and Martin E Newell. Texture and reflection in computer generated images. *Communications of the ACM*, 19(10):542–547, 1976. 3

[9] Timo Bolkart, Tianye Li, and Michael J Black. Instant multi-view head capture through learnable registration. In *Proceedings of the IEEE/CVF Conference on Computer Vision and Pattern Recognition*, pages 768–779, 2023. 3

[10] James Booth, Anastasios Roussos, Stefanos Zafeiriou, Allan Ponniah, and David Dunaway. A 3d morphable model learnt from 10,000 faces. In *Proceedings of the IEEE conference on computer vision and pattern recognition*, pages 5543–5552, 2016. 3

[11] Marcel C Buehler, Gengyan Li, Erroll Wood, Leonhard Helminger, Xu Chen, Tanmay Shah, Daoye Wang, Stephan Garbin, Sergio Orts-Escolano, Otmar Hilliges, et al. Cafca: High-quality novel view synthesis of expressive faces from casual few-shot captures. In *SIGGRAPH Asia 2024 Conference Papers*, pages 1–12, 2024. 3

[12] Marcel C Buehler, Kripasindhu Sarkar, Tanmay Shah, Gengyan Li, Daoye Wang, Leonhard Helminger, Sergio Orts-Escolano, Dmitry Lagun, Otmar Hilliges, Thabo Beeler, et al. Preface: A data-driven volumetric prior for few-shot ultra high-resolution face synthesis. In *Proceedings of the IEEE/CVF International Conference on Computer Vision*, pages 3402–3413, 2023. 3

[13] Chen Cao, Yanlin Weng, Shun Zhou, Yiyong Tong, and Kun Zhou. Facewarehouse: A 3d facial expression database for visual computing. *IEEE Transactions on Visualization and Computer Graphics*, 20(3):413–425, 2013. 3

[14] Chen Cao, Tomas Simon, Jin Kyu Kim, Gabe Schwartz, Michael Zollhoefer, Shun-Suke Saito, Stephen Lombardi,

- Shih-En Wei, Danielle Belko, Shou-I Yu, et al. Authentic volumetric avatars from a phone scan. *ACM Transactions on Graphics (TOG)*, 41(4):1–19, 2022. 3
- [15] Zenghao Chai, Tianke Zhang, Tianyu He, Xu Tan, Tadas Baltrusaitis, HsiangTao Wu, Runnan Li, Sheng Zhao, Chun Yuan, and Jiang Bian. Hiface: High-fidelity 3d face reconstruction by learning static and dynamic details. In *Proceedings of the IEEE/CVF International Conference on Computer Vision*, pages 9087–9098, 2023. 3
- [16] Sumit Chaturvedi, Mengwei Ren, Yannick Hold-Geoffroy, Jingyuan Liu, Julie Dorsey, and Zhixin Shu. Synthlight: Portrait relighting with diffusion model by learning to render synthetic faces. In *Proceedings of the Computer Vision and Pattern Recognition Conference*, pages 369–379, 2025. 16
- [17] Yufan Chen, Lizhen Wang, Qijing Li, Hongjiang Xiao, Shengping Zhang, Hongxun Yao, and Yebin Liu. Mono-gaussianavatar: Monocular gaussian point-based head avatar. In *ACM SIGGRAPH 2024 Conference Papers*, pages 1–9, 2024. 3
- [18] Bowen Cheng, Ishan Misra, Alexander G. Schwing, Alexander Kirillov, and Rohit Girdhar. Masked-attention mask transformer for universal image segmentation. 2022. 6, 11
- [19] Xuangeng Chu and Tatsuya Harada. Generalizable and animatable gaussian head avatar. *Advances in Neural Information Processing Systems*, 37:57642–57670, 2024. 3
- [20] Joon Son Chung, Arsha Nagrani, and Andrew Senior. Voxceleb2: Deep speaker recognition. *arXiv preprint arXiv:1806.05622*, 2018. 3
- [21] Armand Comas-Massagué, Di Qiu, Menglei Chai, Marcel Bühler, Amit Raj, Ruiqi Gao, Qiangeng Xu, Mark Matthews, Paulo Gotardo, Sergio Orts-Escolano, et al. Magicmirror: Fast and high-quality avatar generation with a constrained search space. In *European Conference on Computer Vision*, pages 178–196. Springer, 2024. 1, 3
- [22] MMSegmentation Contributors. MMSegmentation: Openmmlab semantic segmentation toolbox and benchmark. <https://github.com/open-mmlab/mms Segmentation>, 2020. 11
- [23] Paul Debevec. Rendering synthetic objects into real scenes: Bridging traditional and image-based graphics with global illumination and high dynamic range photography. In *Acm siggraph 2008 classes*, pages 1–10. 2008. 3
- [24] Paul Debevec, Tim Hawkins, Chris Tchou, Haarm-Pieter Duiker, Westley Sarokin, and Mark Sagar. Acquiring the reflectance field of a human face. In *Proceedings of the 27th annual conference on Computer graphics and interactive techniques*, pages 145–156, 2000. 3
- [25] Google DeepMind. Veo: Google’s next-generation generative video model. <https://deepmind.google/models/veo/>, 2024. Accessed: 2025-03-29. 14
- [26] Yu Deng, Jiaolong Yang, Sicheng Xu, Dong Chen, Yunde Jia, and Xin Tong. Accurate 3d face reconstruction with weakly-supervised learning: From single image to image set. In *Proceedings of the IEEE/CVF conference on computer vision and pattern recognition workshops*, pages 0–0, 2019. 3
- [27] Mathieu Desbrun, Mark Meyer, Peter Schröder, and Alan H Barr. Implicit fairing of irregular meshes using diffusion and curvature flow. In *Proceedings of the 26th annual conference on Computer graphics and interactive techniques*, pages 317–324, 1999. 5
- [28] Abdallah Dib, Gaurav Bharaj, Junghyun Ahn, Cédric Thébault, Philippe Gosselin, Marco Romeo, and Louis Chevallier. Practical face reconstruction via differentiable ray tracing. In *Computer Graphics Forum*, pages 153–164. Wiley Online Library, 2021. 3, 12, 13
- [29] Abdallah Dib, Junghyun Ahn, Cedric Thebault, Philippe-Henri Gosselin, and Louis Chevallier. S2f2: Self-supervised high fidelity face reconstruction from monocular image. In *2023 IEEE 17th International Conference on Automatic Face and Gesture Recognition (FG)*, pages 1–8. IEEE, 2023. 3
- [30] Hao-Bin Duan, Miao Wang, Jin-Chuan Shi, Xu-Chuan Chen, and Yan-Pei Cao. Bakedavatar: Baking neural fields for real-time head avatar synthesis. *ACM Transactions on Graphics (ToG)*, 42(6):1–17, 2023. 3
- [31] Epic Games. Metahuman creator. <https://dev.epicgames.com/documentation/en-us/metahuman/metahuman-creator>, 2025. Accessed: 2025-07-15. 11
- [32] Epic Games. Mesh to metahuman, 2025. Accessed: 2025-07-07. 10
- [33] Epic Games. MetaHuman. <https://www.unrealengine.com/en-US/metahuman>, 2025. Accessed: 2025-05-13. 2, 8
- [34] Guy Gafni, Justus Thies, Michael Zollhofer, and Matthias Nießner. Dynamic neural radiance fields for monocular 4d facial avatar reconstruction. In *Proceedings of the IEEE/CVF Conference on Computer Vision and Pattern Recognition*, pages 8649–8658, 2021. 3
- [35] Epic Games. Metahuman animator, n.d. Accessed: November 11, 2025. 5
- [36] Xuan Gao, Chenglai Zhong, Jun Xiang, Yang Hong, Yudong Guo, and Juyong Zhang. Reconstructing personalized semantic facial nerf models from monocular video. *ACM Transactions on Graphics (TOG)*, 41(6):1–12, 2022. 3
- [37] Pablo Garrido, Levi Valgaerts, Chenglei Wu, and Christian Theobalt. Reconstructing detailed dynamic face geometry from monocular video. *ACM Trans. Graph.*, 32(6):158–1, 2013. 3
- [38] Pablo Garrido, Michael Zollhöfer, Dan Casas, Levi Valgaerts, Kiran Varanasi, Patrick Pérez, and Christian Theobalt. Reconstruction of personalized 3d face rigs from monocular video. *ACM Transactions on Graphics (TOG)*, 35(3):1–15, 2016. 3
- [39] Abhijeet Ghosh, Graham Fyffe, Borom Tunwattanapong, Jay Busch, Xueming Yu, and Paul Debevec. Multiview face capture using polarized spherical gradient illumination. In *Proceedings of the 2011 SIGGRAPH Asia Conference*, pages 1–10, 2011. 3
- [40] Simon Giebenhain, Tobias Kirschstein, Markos Georgopoulos, Martin Rünz, Lourdes Agapito, and Matthias Nießner. Monophm: Dynamic head reconstruction from monocular videos. In *Proceedings of the IEEE/CVF Conference*

- on *Computer Vision and Pattern Recognition*, pages 10747–10758, 2024. 3
- [41] Ian Goodfellow, Jean Pouget-Abadie, Mehdi Mirza, Bing Xu, David Warde-Farley, Sherjil Ozair, Aaron Courville, and Yoshua Bengio. Generative adversarial networks. *Communications of the ACM*, 63(11):139–144, 2020. 3
- [42] Philip-William Grassal, Malte Prinzler, Titus Leistner, Carsten Rother, Matthias Nießner, and Justus Thies. Neural head avatars from monocular rgb videos. In *Proceedings of the IEEE/CVF conference on computer vision and pattern recognition*, pages 18653–18664, 2022. 3, 12, 13
- [43] Antoine Guédon and Vincent Lepetit. Sugar: Surface-aligned gaussian splatting for efficient 3d mesh reconstruction and high-quality mesh rendering. In *Proceedings of the IEEE/CVF Conference on Computer Vision and Pattern Recognition*, pages 5354–5363, 2024. 5
- [44] Yuxuan Han, Junfeng Lyu, and Feng Xu. High-quality facial geometry and appearance capture at home. In *Proceedings of the IEEE/CVF Conference on Computer Vision and Pattern Recognition*, pages 697–707, 2024. 3, 13
- [45] Yisheng He, Xiaodong Gu, Xiaodan Ye, Chao Xu, Zhengyi Zhao, Yuan Dong, Weihao Yuan, Zilong Dong, and Liefeng Bo. Lam: Large avatar model for one-shot animatable gaussian head. In *Proceedings of the Special Interest Group on Computer Graphics and Interactive Techniques Conference Conference Papers*, pages 1–13, 2025. 3
- [46] Sebastian Herholz, Timo Schairer, and Wolfgang Straßer. Screen space spherical harmonics occlusion (s3ho) sampling. In *ACM SIGGRAPH 2011 Posters*, pages 1–1. 2011. 9
- [47] Yang Hong, Bo Peng, Haiyao Xiao, Ligang Liu, and Juyong Zhang. Headnerf: A real-time nerf-based parametric head model. In *Proceedings of the IEEE/CVF Conference on Computer Vision and Pattern Recognition*, pages 20374–20384, 2022. 3
- [48] Andrew Hou, Ze Zhang, Michel Sarkis, Ning Bi, Yiyong Tong, and Xiaoming Liu. Towards high fidelity face relighting with realistic shadows. In *Proceedings of the IEEE/CVF conference on computer vision and pattern recognition*, pages 14719–14728, 2021. 3
- [49] Andrew Hou, Michel Sarkis, Ning Bi, Yiyong Tong, and Xiaoming Liu. Face relighting with geometrically consistent shadows. In *Proceedings of the IEEE/CVF conference on computer vision and pattern recognition*, pages 4217–4226, 2022. 3
- [50] Binbin Huang, Zehao Yu, Anpei Chen, Andreas Geiger, and Shenghua Gao. 2d gaussian splatting for geometrically accurate radiance fields. In *SIGGRAPH 2024 Conference Papers*. Association for Computing Machinery, 2024. 5
- [51] Kaiwen Jiang, Shu-Yu Chen, Feng-Lin Liu, Hongbo Fu, and Lin Gao. Nerffacediting: Disentangled face editing in neural radiance fields. In *SIGGRAPH Asia 2022 Conference Papers*, pages 1–9, 2022. 3
- [52] Hendrik Junkawitsch, Guoxing Sun, Heming Zhu, Christian Theobalt, and Marc Habermann. Eva: Expressive virtual avatars from multi-view videos. In *Proceedings of the Special Interest Group on Computer Graphics and Interactive Techniques Conference Conference Papers*, pages 1–11, 2025. 15
- [53] Bernhard Kerbl, Georgios Kopanas, Thomas Leimkühler, and George Drettakis. 3d gaussian splatting for real-time radiance field rendering. *ACM Trans. Graph.*, 42(4):139–1, 2023. 1, 4, 10, 11
- [54] Hoon Kim, Minje Jang, Wonjun Yoon, Jisoo Lee, Donghyun Na, and Sanghyun Woo. Switchlight: Co-design of physics-driven architecture and pre-training framework for human portrait relighting. In *Proceedings of the IEEE/CVF Conference on Computer Vision and Pattern Recognition*, pages 25096–25106, 2024. 3, 15, 16
- [55] Diederik P Kingma and Jimmy Ba. Adam: A method for stochastic optimization. *arXiv preprint arXiv:1412.6980*, 2014. 11
- [56] Tatsuro Koizumi and William AP Smith. “look ma, no landmarks!”—unsupervised, model-based dense face alignment. In *European Conference on Computer Vision*, pages 690–706. Springer, 2020. 3
- [57] Alexandros Lattas, Stylianos Moschoglou, Baris Gecer, Stylianos Ploumpis, Vasileios Triantafyllou, Abhijeet Ghosh, and Stefanos Zafeiriou. Avatarme: Realistically renderable 3d facial reconstruction” in-the-wild”. In *Proceedings of the IEEE/CVF conference on computer vision and pattern recognition*, pages 760–769, 2020. 3
- [58] Alexandros Lattas, Stylianos Moschoglou, Stylianos Ploumpis, Baris Gecer, Abhijeet Ghosh, and Stefanos Zafeiriou. Avatarme++: Facial shape and brdf inference with photorealistic rendering-aware gans. *IEEE Transactions on Pattern Analysis and Machine Intelligence*, 44(12):9269–9284, 2021. 3
- [59] Eric Lengyel. *Mathematics for 3D Game Programming and Computer Graphics*. Cengage Learning PTR, Florence, KY, 2 edition, 2003. 6
- [60] Jianhui Li, Shilong Liu, Zidong Liu, Yikai Wang, Kaiwen Zheng, Jinghui Xu, Jianmin Li, and Jun Zhu. Instructpix2nerf: instructed 3d portrait editing from a single image. *arXiv preprint arXiv:2311.02826*, 2023. 3
- [61] Junxuan Li, Chen Cao, Gabriel Schwartz, Rawal Khirodkar, Christian Richardt, Tomas Simon, Yaser Sheikh, and Shunsuke Saito. Uravatar: Universal relightable gaussian codec avatars. In *SIGGRAPH Asia 2024 Conference Papers*, pages 1–11, 2024. 3, 4
- [62] Ruilong Li, Karl Bladin, Yajie Zhao, Chinmay Chinara, Owen Ingraham, Pengda Xiang, Xinglei Ren, Pratusha Prasad, Bipin Kishore, Jun Xing, et al. Learning formation of physically-based face attributes. In *Proceedings of the IEEE/CVF conference on computer vision and pattern recognition*, pages 3410–3419, 2020. 3
- [63] Tianye Li, Timo Bolkart, Michael J Black, Hao Li, and Javier Romero. Learning a model of facial shape and expression from 4d scans. *ACM Trans. Graph.*, 36(6):194–1, 2017. 3
- [64] Xuanchen Li, Yuhao Cheng, Xingyu Ren, Haozhe Jia, Di Xu, Wenhan Zhu, and Yichao Yan. Topo4d: Topology-preserving gaussian splatting for high-fidelity 4d head capture. In *European Conference on Computer Vision*, pages 128–145. Springer, 2024. 3, 6
- [65] Tingting Liao, Yujian Zheng, Yuliang Xiu, Adilbek Kermanov, Liwen Hu, Leyang Jin, and Hao Li. Soap: Style-omniscient animatable portraits. In *Proceedings of the*

- Special Interest Group on Computer Graphics and Interactive Techniques Conference Conference Papers*, pages 1–11, 2025. 3
- [66] Connor Z Lin, David B Lindell, Eric R Chan, and Gordon Wetzstein. 3d gan inversion for controllable portrait image animation. *arXiv preprint arXiv:2203.13441*, 2022. 3
- [67] Winnie Lin, Yilin Zhu, Demi Guo, and Ron Fedkiw. Leveraging deepfakes to close the domain gap between real and synthetic images in facial capture pipelines. *arXiv preprint arXiv:2204.10746*, 2022. 10, 15
- [68] Xiangyue Liu, Kunming Luo, Heng Li, Qi Zhang, Yuan Liu, Li Yi, and Ping Tan. Gaussianavatar-editor: Photorealistic animatable gaussian head avatar editor, 2025. 3
- [69] Ziwei Liu, Ping Luo, Xiaogang Wang, and Xiaoou Tang. Deep learning face attributes in the wild. In *Proceedings of the IEEE international conference on computer vision*, pages 3730–3738, 2015. 3
- [70] Shugao Ma, Tomas Simon, Jason Saragih, Dawei Wang, Yuecheng Li, Fernando De La Torre, and Yaser Sheikh. Pixel codec avatars. In *Proceedings of the IEEE/CVF Conference on Computer Vision and Pattern Recognition*, pages 64–73, 2021. 3
- [71] Wan-Chun Ma, Tim Hawkins, Pieter Peers, Charles-Felix Chabert, Malte Weiss, Paul E Debevec, et al. Rapid acquisition of specular and diffuse normal maps from polarized spherical gradient illumination. *Rendering Techniques*, 9(10):2, 2007. 3
- [72] Debin Meng, Christos Tzelepis, Ioannis Patras, and Georgios Tzimiropoulos. Mm2latent: Text-to-facial image generation and editing in gans with multimodal assistance. In *European Conference on Computer Vision*, pages 88–106. Springer, 2024. 16
- [73] Maxwell Meyer and Jack Spruyt. Ben: Using confidence-guided matting for dichotomous image segmentation. *arXiv preprint arXiv:2501.06230*, 2025. 6
- [74] Ben Mildenhall, Pratul P Srinivasan, Matthew Tancik, Jonathan T Barron, Ravi Ramamoorthi, and Ren Ng. Nerf: Representing scenes as neural radiance fields for view synthesis. *Communications of the ACM*, 65(1):99–106, 2021. 1
- [75] Gene S Miller and CR Hoffman. Illumination and reflection maps. In *ACM SIGGRAPH*, 1984. 3
- [76] Thomas Nestmeyer, Jean-François Lalonde, Iain Matthews, and Andreas Lehrmann. Learning physics-guided face relighting under directional light. In *Proceedings of the IEEE/CVF Conference on Computer Vision and Pattern Recognition*, pages 5124–5133, 2020. 3
- [77] OpenAI. Chatgpt (sept 12 version). <https://chat.openai.com/>, 2025. Large language model. 14
- [78] Rohit Pandey, Sergio Orts-Escolano, Chloe Legendre, Christian Haene, Sofien Bouaziz, Christoph Rhemann, Paul E Debevec, and Sean Ryan Fanello. Total relighting: learning to relight portraits for background replacement. *ACM Trans. Graph.*, 40(4):43–1, 2021. 3
- [79] Pascal Paysan, Reinhard Knothe, Brian Amberg, Sami Romdhani, and Thomas Vetter. A 3d face model for pose and illumination invariant face recognition. In *2009 sixth IEEE international conference on advanced video and signal based surveillance*, pages 296–301. Ieee, 2009. 3
- [80] José Luis Pech-Pacheco, Gabriel Cristóbal, Jesús Chamorro-Martínez, and Joaquín Fernández-Valdivia. Diatom auto-focusing in brightfield microscopy: a comparative study. In *Proceedings 15th International Conference on Pattern Recognition. ICPR-2000*, pages 314–317. IEEE, 2000. 5
- [81] Shenhan Qian, Tobias Kirschstein, Liam Schoneveld, Davide Davoli, Simon Giebenhain, and Matthias Nießner. Gaussianavatars: Photorealistic head avatars with rigged 3d gaussians. In *Proceedings of the IEEE/CVF Conference on Computer Vision and Pattern Recognition*, pages 20299–20309, 2024. 3, 4, 5, 6, 11
- [82] Ravi Ramamoorthi and Pat Hanrahan. An efficient representation for irradiance environment maps. In *Proceedings of the 28th annual conference on Computer graphics and interactive techniques*, pages 497–500, 2001. 8
- [83] Chirag Raman, Charlie Hewitt, Erroll Wood, and Tadas Baltrušaitis. Mesh-tension driven expression-based wrinkles for synthetic faces. In *Proceedings of the IEEE/CVF Winter Conference on Applications of Computer Vision*, pages 3515–3525, 2023. 3
- [84] Pramod Rao, Gereon Fox, Abhimitra Meka, Mallikarjun BR, Fangneng Zhan, Tim Weyrich, Bernd Bickel, Hanspeter Pfister, Wojciech Matusik, Mohamed Elgharib, et al. Lite2relight: 3d-aware single image portrait relighting. In *ACM SIGGRAPH 2024 Conference Papers*, pages 1–12, 2024. 16
- [85] Elad Richardson, Matan Sela, and Ron Kimmel. 3d face reconstruction by learning from synthetic data. In *2016 fourth international conference on 3D vision (3DV)*, pages 460–469. IEEE, 2016. 3
- [86] Christos Sagonas, Epameinondas Antonakos, Georgios Tzimiropoulos, Stefanos Zafeiriou, and Maja Pantic. 300 faces in-the-wild challenge: Database and results. *Image and vision computing*, 47:3–18, 2016. 3
- [87] Shunsuke Saito, Gabriel Schwartz, Tomas Simon, Junxuan Li, and Giljoo Nam. Relightable gaussian codec avatars. In *Proceedings of the IEEE/CVF conference on computer vision and pattern recognition*, pages 130–141, 2024. 3, 4, 9, 10
- [88] Kripasindhu Sarkar, Marcel C Bühler, Gengyan Li, Daoye Wang, Delio Vicini, Jérémy Riviere, Yinda Zhang, Sergio Orts-Escolano, Paulo Gotardo, Thabo Beeler, et al. Litnerf: Intrinsic radiance decomposition for high-quality view synthesis and relighting of faces. In *SIGGRAPH Asia 2023 Conference Papers*, pages 1–11, 2023. 3
- [89] Jack Saunders, Charlie Hewitt, Yanan Jian, Marek Kowalski, Tadas Baltrušaitis, Yiye Chen, Darren Cosker, Virginia Estellers, Nicholas Gyde, Vinay P. Nambodiri, and Benjamin E Lundell. Gasp: Gaussian avatars with synthetic priors, 2024. 3
- [90] Zhijing Shao, Zhaolong Wang, Zhuang Li, Duotun Wang, Xiangru Lin, Yu Zhang, Mingming Fan, and Zeyu Wang. Splattingavatar: Realistic real-time human avatars with mesh-embedded gaussian splatting. In *Proceedings of the IEEE/CVF Conference on Computer Vision and Pattern Recognition*, pages 1606–1616, 2024. 3

- [91] Heyi Sun, Cong Wang, Tian-Xing Xu, Jingwei Huang, Di Kang, Chunchao Guo, and Song-Hai Zhang. Svg-head: Hybrid surface-volumetric gaussians for high-fidelity head reconstruction and real-time editing. In *Proceedings of the IEEE/CVF International Conference on Computer Vision*, pages 13326–13335, 2025. 3
- [92] Jingxiang Sun, Xuan Wang, Yong Zhang, Xiaoyu Li, Qi Zhang, Yebin Liu, and Jue Wang. Fenerf: Face editing in neural radiance fields. In *Proceedings of the IEEE/CVF conference on computer vision and pattern recognition*, pages 7672–7682, 2022. 3
- [93] Tiancheng Sun, Jonathan T Barron, Yun-Ta Tsai, Zexiang Xu, Xueming Yu, Graham Fyffe, Christoph Rhemann, Jay Busch, Paul E Debevec, and Ravi Ramamoorthi. Single image portrait relighting. *ACM Trans. Graph.*, 38(4):79–1, 2019. 3
- [94] Kartik Teotia, Hyeonwoo Kim, Pablo Garrido, Marc Habermann, Mohamed Elgharib, and Christian Theobalt. Gaussianheads: End-to-end learning of drivable gaussian head avatars from coarse-to-fine representations. *ACM Transactions on Graphics (TOG)*, 43(6):1–12, 2024. 3
- [95] Kartik Teotia, Xingang Pan, Hyeonwoo Kim, Pablo Garrido, Mohamed Elgharib, and Christian Theobalt. Hq3davatar: High-quality implicit 3d head avatar. *ACM Transactions on Graphics*, 43(3):1–24, 2024. 3
- [96] Ayush Tewari, Michael Zollhoefer, Florian Bernard, Pablo Garrido, Hyeonwoo Kim, Patrick Perez, and Christian Theobalt. High-fidelity monocular face reconstruction based on an unsupervised model-based face autoencoder. *IEEE transactions on pattern analysis and machine intelligence*, 42(2):357–370, 2018. 3
- [97] Ayush Tewari, Florian Bernard, Pablo Garrido, Gaurav Bharaj, Mohamed Elgharib, Hans-Peter Seidel, Patrick Pérez, Michael Zollhofer, and Christian Theobalt. Fml: Face model learning from videos. In *Proceedings of the IEEE/CVF Conference on Computer Vision and Pattern Recognition*, pages 10812–10822, 2019. 3
- [98] Justus Thies, Michael Zollhöfer, and Matthias Nießner. Deferred neural rendering: Image synthesis using neural textures. *Acm Transactions on Graphics (TOG)*, 38(4):1–12, 2019. 3
- [99] Luan Tran and Xiaoming Liu. Nonlinear 3d face morphable model. In *Proceedings of the IEEE conference on computer vision and pattern recognition*, pages 7346–7355, 2018. 3
- [100] Luan Tran, Feng Liu, and Xiaoming Liu. Towards high-fidelity nonlinear 3d face morphable model. In *Proceedings of the IEEE/CVF Conference on Computer Vision and Pattern Recognition*, pages 1126–1135, 2019. 3
- [101] Alex Trevithick, Matthew Chan, Michael Stengel, Eric Chan, Chao Liu, Zhiding Yu, Sameh Khamis, Manmohan Chandraker, Ravi Ramamoorthi, and Koki Nagano. Real-time radiance fields for single-image portrait view synthesis. *ACM Transactions on Graphics (TOG)*, 42(4):1–15, 2023. 3
- [102] Cong Wang, Di Kang, He-Yi Sun, Shen-Han Qian, Zi-Xuan Wang, Linchao Bao, and Song-Hai Zhang. Mega: Hybrid mesh-gaussian head avatar for high-fidelity rendering and head editing. *arXiv preprint arXiv:2404.19026*, 2024. 3, 15
- [103] Jie Wang, Jiu-Cheng Xie, Xianyan Li, Feng Xu, Chi-Man Pun, and Hao Gao. Gaussianhead: High-fidelity head avatars with learnable gaussian derivation. *arXiv preprint arXiv:2312.01632*, 2023. 3
- [104] Lizhen Wang, Zhiyuan Chen, Tao Yu, Chenguang Ma, Liang Li, and Yebin Liu. Faceverse: a fine-grained and detail-controllable 3d face morphable model from a hybrid dataset. In *Proceedings of the IEEE/CVF conference on computer vision and pattern recognition*, pages 20333–20342, 2022. 3
- [105] Yifan Wang, Aleksander Holynski, Xiuming Zhang, and Xuaner Zhang. Sunstage: Portrait reconstruction and relighting using the sun as a light stage. In *Proceedings of the IEEE/CVF Conference on Computer Vision and Pattern Recognition*, pages 20792–20802, 2023. 4
- [106] Zhou Wang, Alan C Bovik, Hamid R Sheikh, and Eero P Simoncelli. Image quality assessment: from error visibility to structural similarity. *IEEE transactions on image processing*, 13(4):600–612, 2004. 11
- [107] Zhibo Wang, Xin Yu, Ming Lu, Quan Wang, Chen Qian, and Feng Xu. Single image portrait relighting via explicit multiple reflectance channel modeling. *ACM Transactions on Graphics (ToG)*, 39(6):1–13, 2020. 3
- [108] Erroll Wood, Tadas Baltrušaitis, Charlie Hewitt, Sebastian Dziadzio, Thomas J Cashman, and Jamie Shotton. Fake it till you make it: face analysis in the wild using synthetic data alone. In *Proceedings of the IEEE/CVF international conference on computer vision*, pages 3681–3691, 2021. 3
- [109] Erroll Wood, Tadas Baltrušaitis, Charlie Hewitt, Matthew Johnson, Jingjing Shen, Nikola Milosavljević, Daniel Wilde, Stephan Garbin, Toby Sharp, Ivan Stojiljković, et al. 3d face reconstruction with dense landmarks. In *European Conference on Computer Vision*, pages 160–177. Springer, 2022. 3
- [110] Jun Xiang, Xuan Gao, Yudong Guo, and Juyong Zhang. Flashavatar: High-fidelity head avatar with efficient gaussian embedding. In *Proceedings of the IEEE/CVF Conference on Computer Vision and Pattern Recognition*, pages 1802–1812, 2024. 3
- [111] Yuelang Xu, Benwang Chen, Zhe Li, Hongwen Zhang, Lizhen Wang, Zerong Zheng, and Yebin Liu. Gaussian head avatar: Ultra high-fidelity head avatar via dynamic gaussians. In *Proceedings of the IEEE/CVF conference on computer vision and pattern recognition*, pages 1931–1941, 2024. 3
- [112] Shugo Yamaguchi, Shunsuke Saito, Koki Nagano, Yajie Zhao, Weikai Chen, Kyle Olszewski, Shigeo Morishima, and Hao Li. High-fidelity facial reflectance and geometry inference from an unconstrained image. *ACM Transactions on Graphics (TOG)*, 37(4):1–14, 2018. 3
- [113] Haotian Yang, Hao Zhu, Yanru Wang, Mingkai Huang, Qiu Shen, Ruigang Yang, and Xun Cao. Facescape: a large-scale high quality 3d face dataset and detailed riggable 3d face prediction. In *Proceedings of the IEEE/CVF conference on computer vision and pattern recognition*, pages 601–610, 2020. 3
- [114] Haotian Yang, Mingwu Zheng, Chongyang Ma, Yu-Kun Lai, Pengfei Wan, and Haibin Huang. Vrmm: A volumetric

- relightable morphable head model. In *ACM SIGGRAPH 2024 Conference Papers*, pages 1–11, 2024. 3
- [115] Tarun Yenamandra, Ayush Tewari, Florian Bernard, Hans-Peter Seidel, Mohamed Elgharib, Daniel Cremers, and Christian Theobalt. i3dmm: Deep implicit 3d morphable model of human heads. In *Proceedings of the IEEE/CVF Conference on Computer Vision and Pattern Recognition*, pages 12803–12813, 2021. 3
- [116] Lijun Yin, Xiaozhou Wei, Yi Sun, Jun Wang, and Matthew J Rosato. A 3d facial expression database for facial behavior research. In *7th international conference on automatic face and gesture recognition (FGR06)*, pages 211–216. IEEE, 2006. 3
- [117] Jiawei Zhang, Zijian Wu, Zhiyang Liang, Yicheng Gong, Dongfang Hu, Yao Yao, Xun Cao, and Hao Zhu. Fate: Full-head gaussian avatar with textural editing from monocular video. In *Proceedings of the Computer Vision and Pattern Recognition Conference*, pages 5535–5545, 2025. 15
- [118] Tianke Zhang, Xuangeng Chu, Yunfei Liu, Lijian Lin, Zhendong Yang, Zhengzhuo Xu, Chengkun Cao, Fei Yu, Changyin Zhou, Chun Yuan, et al. Accurate 3d face reconstruction with facial component tokens. In *Proceedings of the IEEE/CVF international conference on computer vision*, pages 9033–9042, 2023. 3
- [119] Xinjie Zhang, Xingtong Ge, Tongda Xu, Dailan He, Yan Wang, Hongwei Qin, Guo Lu, Jing Geng, and Jun Zhang. Gaussianimage: 1000 fps image representation and compression by 2d gaussian splatting. In *European Conference on Computer Vision*, 2024. 8
- [120] Hang Zhao, Orazio Gallo, Iuri Frosio, and Jan Kautz. Loss functions for image restoration with neural networks. *IEEE Transactions on computational imaging*, 3(1):47–57, 2016. 11
- [121] Zhongyuan Zhao, Zhenyu Bao, Qing Li, Guoping Qiu, and Kanglin Liu. Psavatar: a point-based morphable shape model for real-time head avatar creation with 3d gaussian splatting. *arXiv e-prints*, pages arXiv–2401, 2024. 3
- [122] Yufeng Zheng, Victoria Fernández Abrevaya, Marcel C Bühler, Xu Chen, Michael J Black, and Otmar Hilliges. Im avatar: Implicit morphable head avatars from videos. In *Proceedings of the IEEE/CVF conference on computer vision and pattern recognition*, pages 13545–13555, 2022. 3
- [123] Yufeng Zheng, Wang Yifan, Gordon Wetzstein, Michael J Black, and Otmar Hilliges. Pointavatar: Deformable point-based head avatars from videos. In *Proceedings of the IEEE/CVF conference on computer vision and pattern recognition*, pages 21057–21067, 2023. 3, 4
- [124] Hao Zhou, Sunil Hadap, Kalyan Sunkavalli, and David W Jacobs. Deep single-image portrait relighting. In *Proceedings of the IEEE/CVF international conference on computer vision*, pages 7194–7202, 2019. 3
- [125] Xiangyu Zhu, Zhen Lei, Xiaoming Liu, Hailin Shi, and Stan Z Li. Face alignment across large poses: A 3d solution. In *Proceedings of the IEEE conference on computer vision and pattern recognition*, pages 146–155, 2016. 3
- [126] Yilin Zhu, Dalton Omens, Haodi He, and Ron Fedkiw. Democratizing the creation of animatable facial avatars, 2024. 10
- [127] Yiyu Zhuang, Hao Zhu, Xusen Sun, and Xun Cao. Mofan-erf: Morphable facial neural radiance field. In *European conference on computer vision*, pages 268–285. Springer, 2022. 3
- [128] Wojciech Zielonka, Timo Bolkart, and Justus Thies. Instant volumetric head avatars. In *Proceedings of the IEEE/CVF conference on computer vision and pattern recognition*, pages 4574–4584, 2023. 3